



저작자표시-비영리-변경금지 2.0 대한민국

이용자는 아래의 조건을 따르는 경우에 한하여 자유롭게

- 이 저작물을 복제, 배포, 전송, 전시, 공연 및 방송할 수 있습니다.

다음과 같은 조건을 따라야 합니다:



저작자표시. 귀하는 원저작자를 표시하여야 합니다.



비영리. 귀하는 이 저작물을 영리 목적으로 이용할 수 없습니다.



변경금지. 귀하는 이 저작물을 개작, 변형 또는 가공할 수 없습니다.

- 귀하는, 이 저작물의 재이용이나 배포의 경우, 이 저작물에 적용된 이용허락조건을 명확하게 나타내어야 합니다.
- 저작권자로부터 별도의 허가를 받으면 이러한 조건들은 적용되지 않습니다.

저작권법에 따른 이용자의 권리는 위의 내용에 의하여 영향을 받지 않습니다.

이것은 [이용허락규약\(Legal Code\)](#)을 이해하기 쉽게 요약한 것입니다.

[Disclaimer](#)

工學博士學位論文

**Fabrication of Uniform Hierarchical Mesoporous
Wrinkled Silica Nanoparticles and Their
Applications: Chemical Mechanical Planarization,
Solar Cell, and Electrorheological Fluid**

**균일한 다공성 주름진 실리카 나노입자의 제조와 응용:
화학적 기계적 평탄화, 태양 전지, 전기유변유체**

2018年 2月

서울대학교 大學院

化學生物工學部

柳 在 勳

<div>Fabrication of Uniform Hierarchical Mesoporous Wrinkled Silica Nanoparticles and Their Applications: Chemical Mechanical Planarization, Solar Cell, and Electrotheological Fluid</div>					
<div>2018年柳在勳</div>					
<div>↑ 2cm ↓</div>		<div>↑ 2.5cm ↓</div>		<div>↑ 4cm ↓</div>	
		<div>↑ 3cm ↓</div>		<div>↑ 2cm ↓</div>	

Attn: President of Seoul National University

**Fabrication of Uniform Hierarchical Mesoporous
Wrinkled Silica Nanoparticles and Their
Applications: Chemical Mechanical Planarization,
Solar Cell, and Electrorheological Fluid**

by

Jaehoon Ryu

Submitted to the Graduate School of Seoul National University in
Partial Fulfillment of the Requirements for the Degree of Doctor
of Philosophy

February, 2018

Thesis Adviser: Jyongsik Jang

Abstract

Mesoporous silica nanomaterials have received much attention due to their dramatic increased surface to volume ratio. These porous structures have been used extensively in a variety of applications such as catalyst supporters, adsorption, separation, drug delivery, electrodes, and hard templates for fabrication of nanocomposites due to their unique features. Among various structures of mesoporous silica nanomaterials, spherical mesoporous silica nanoparticles have attracted much attention because they provide excellent pore accessibility and smooth molecular diffusion. Therefore, various methods for the fabrication of spherical mesoporous silica nanoparticles with a range of pore structure types have been reported, and have contributed to the development of fields such as packing materials for chromatography, drug delivery, cosmetics, and adsorption. However, despite the variety of methods for preparing spherical mesoporous silica nanoparticles, it should be still required to develop fabrication methods of spherical mesoporous silica nanoparticles with uniformity and high yields.

This dissertation introduces a method for fabricating uniform hierarchical mesoporous wrinkled silica nanoparticles. Furthermore,

formation mechanism of the uniform spherical mesoporous silica nanoparticles was discussed by investigating the factors affecting the particle size and pore size of the nanoparticles. Thus, a complete method for high-yield production of uniform hierarchical mesoporous wrinkled silica nanoparticles with tunable particle size and pore size is provided. The prepared uniform mesoporous silica nanoparticles manifested better performance than non-porous silica nanoparticles of the same size in applications of abrasives in chemical mechanical planarization, scattering materials in dye sensitized solar cells, and hard templates for fabricating nanocomposite of ER fluids, demonstrating the superiority of the mesoporous structure. This dissertation suggests that silica nanoparticles with mesoporous structure offer the potential for performance enhancement in applications where non-porous silica spheres are currently used.

Keywords: Nanomaterials; Mesoporous silica nanomaterials; Spherical mesoporous silica nanoparticles; Chemical mechanical planarization; Solar cells; Electrorheological fluids.

Student Number: 2013-22528

List of Abbreviations

AFM: atomic force microscopy

BET: Brunauer Emmett Teller

BJH: Barrett–Joyner–Halenda

CMP: chemical mechanical planarization

DRS: diffused reflectance spectra

DSSCs: dye sensitized solar cells

E: Young's modulus

ER: electrorheological

FF: fill factor

FTO: Fluorine-doped tin dioxide

H: hardness

iPA: iso-Propanol

J_{sc} : short-circuit current

MRR: material removal rate

OM: optical microscopy

PCE: power conversion efficiency

QE: quantum efficiency

SEM: scanning electronic microscopy

STEM-EDS: scanning transmission electron microscopy-energy

dispersive spectroscopy

S-HNPs: silica sphere based-SiO₂/TiO₂ hollow nanoparticles

S-STCSs: silica sphere based-SiO₂/TiO₂ core/shell nanoparticles

TEM: transmission electronic microscopy

TTIP: titanium(IV) isopropoxide

V_{oc} : open-circuit voltage

WSNs: hierarchical mesoporous wrinkled silica nanoparticles

W-HNPs: WSN based-SiO₂/TiO₂ hollow nanoparticles

W-STCSs: WSN based-SiO₂/TiO₂ core/shell nanoparticles

List of Figures

- Figure 1.** Routes of chemical fabrication of colloidal silica.
- Figure 2.** Phase regions of microemulsion systems.
- Figure 3.** Schematic representation of four type of Winsor system.
- Figure 4.** Schematic illustration of CMP process.
- Figure 5.** Structure and operating mechanism of a dye-sensitized solar cell.
- Figure 6.** TEM images of WSNs fabricated (a) with and (b) without cooling process. (c) Size distribution profiles of WSNs fabricated with and without cooling process.
- Figure 7.** TEM images of the WSNs reacted at 70 °C for (a) 0, (b) 0.5, (c) 1, and (d) 2 h before cooling process. The reactions of all samples proceed for 6 h at 70 °C after cooling process.
- Figure 8.** The photo picture of the reaction mixtures after cooling process and TEM images of primary particles of WSN.
- Figure 9.** TEM image of the WSNs reacted at 80 °C for 1 h before cooling process. After cooling process, the reaction proceeded for 6 h at 70 °C.

Figure 10. TEM images of WSNs fabricated at 70 °C for (a) 3 h without cooling process and (b) 3 h before cooling, followed by 1 h.

Figure 11. Proposed the uniform WSN forming mechanism with the added cooling process during the reaction.

Figure 12. Effect of reaction time after cooling process; TEM images of the WSNs reacted at 70 °C for (a) 2 h, (b) 3 h, (c) 6 h, and (d) 12 h after 1 h pre-reaction and cooling process. All samples reacted before cooling process for 1 h at 70 °C. (e) Variation of WSN size and WSN yield relative to addition amount of TEOS as function of the reaction time.

Figure 13. TEM image of the WSNs reacted at 70 °C for 16 h after 1 h pre-reaction and cooling process.

Figure 14. Effect of reaction temperature after cooling process; TEM images, SEM images and the corresponding BJH plots of the WSNs reacted at (a, b, c) 70, (d, e, f) 75 °C, and (g, h, i) 80 °C for 12 h after cooling process. All samples reacted before cooling process for 1 h at 70 °C.

Figure 15. N₂ adsorption-desorption isotherms of the WSNs reacted at

(a) 70, (b) 75, and (c) 80 °C for 12 h after cooling process.

All samples reacted before cooling process for 1 hour at 70 °C (corresponding with **Figure. 14**).

Figure 16. Effect of oil-to-water ratio; TEM images and the corresponding pore volume distribution plots of the WSNs fabricated with different oil-to-water ratio, (a, b) = 0.5, and (c, d) = 1

Figure 17. N₂ adsorption-desorption isotherms of the WSNs fabricated with different oil to water ratio, (a) = 0.5, and (b) = 1 in the reaction mixture (corresponding with **Figure. 16**).

Figure 18. Effect of amount of added iso-propanol (iPA); TEM images and the corresponding pore volume distribution plots of the WSNs fabricated with different amounts of iPA, (a, b) 0.92 mL, (c, d) 1.84 mL, and (e, f) 2.76 mL iPA.

Figure 19. N₂ adsorption-desorption isotherms of the WSNs fabricated with different amounts of iPA, (a) 0.92 mL, (b) 1.84 mL, and (c) 2.76 mL iPA (corresponding with **Figure. 18**).

Figure 20. Effect of cosolvent; TEM images, SEM images, and the corresponding pore volume distribution plots of the WSNs fabricated with different cosolvent, (a, b, c) 1.84 ml iPA, (d,

e, f) 2.2 ml butanol, and (g, h, i) 1.1 ml butanol.

Figure 21. N₂ adsorption-desorption isotherms of the WSNs fabricated with (a) 2.2 ml and (b) 1.1 ml butanol (corresponding with **Figure 20**).

Figure 22. (a) Cross-sectional SEM and (b) 3D AFM images of the substrates before CMP process.

Figure 23. Cross-sectional SEM images and 3D AFM images of the substrates after CMP with corresponding TEM images of (a) monodisperse-SiO₂ spheres (100 nm), (b) monodisperse-WSNs (100 nm), and (c) STAR4000 as slurry abrasive materials.

Figure 24. (a) N₂ adsorption-desorption isotherms and (b) pore volume distribution plots of 100 nm silica spheres.

Figure 25. TEM image of WSNs after CMP process.

Figure 26. (a) Schematic illustration and (b) cross-section SEM image of the device structure of DSSCs containing TiO₂ NPs under-layers and WSNs over-layer as a scattering layer.

Figure 27. SEM image of WSNs over-layer as a scattering layer of working electrode in the DSSCs device.

Figure 28. TEM images of (a) 220 nm silica spheres, (b) 220 nm

WSNs, (c) 320 nm WSNs, and (d) 430 nm WSNs.

Figure 29. N_2 adsorption-desorption isotherms and pore volume distribution plots (inset) of (a) 220 nm silica spheres and WSNs with (b) 220 nm, (c) 320 nm, (d) 430 nm diameters.

Figure 30. (a) Diffuse reflectance spectra for 200 nm silica spheres and WSNs with various sizes (220, 320, 430 nm). (b) Schematic illustration of the light scattering effect within spheres and WSNs

Figure 31. (a) Current density-voltage (J–V) characteristics and (b) Incident photon-to-current efficiency (IPCE) spectra for DSSCs based on WSNs with various sizes and 220 nm silica spheres; (c) IPCE enhancement factor ($=IPCE_{\text{sample}} / IPCE_{220\text{spheres}}$) based on the 220 spheres, and (d) DRS enhancement factor ($=DRS_{\text{sample}} / DRS_{220\text{spheres}}$) based on the 220 spheres.

Figure 32. Schematic illustration of the formation mechanism of the WSN-SiO₂/TiO₂ hollow nanoparticles.

Figure 33. Transmission electron microscopy (TEM) images of (a) WSN, (b) W-STCS, and (c) W-HNP. (d) Scanning electron microscopy (SEM) image of W-HNP.

Figure 34. TEM images of (a) the 80nm-diameter-WSNs and (b) W-HNPs fabricated with the 80nm-diameter-WSNs.

Figure 35. TEM images of the W-HNPs fabricated with different amount of TTIP.

Figure 36. STEM-elemental-mapping images of W-HNP.

Figure 37. STEM-elemental-mapping images of WSN.

Figure 38. STEM-elemental-mapping images of W-STCS.

Figure 39. N_2 adsorption-desorption isotherm and pore volume distribution plots of (a, b) WSNs, (c, d) W-STCSs, and (e, f) W-HNPs.

Figure 40. TEM images of (a) SiO_2 spheres, (b) S-STCS, and (c) S-HNPs.

Figure 41. N_2 adsorption-desorption isotherm and pore volume distribution plots of (a, b) Spheres, (c, d) S-STCSs, and (e, f) S-HNPs.

Figure 42. (a) Sedimentation ratio (R) of sphere- and WSN-derived materials-based ER fluids in silicone oil (3.0 wt%) and (b) Graphical illustration and definition of sedimentation ratio.

Figure 43. Dielectric constant (ϵ') and loss factor (ϵ'') of sphere- and WSN-derived material-based ER fluids as a function of

electric field frequency (f).

Figure 44. (a) Electrorheological activities of sphere- and WSN-derived ER fluids WSN, and TiO₂-coated materials as a function of shear rate (3.0 wt%, 3.0 kV mm⁻¹), (b) Proposed mechanism of polarization differences in sphere and WSN materials, (c) Yield stresses of ER fluids measured as a function of E field strength (3.0 wt%, 0.1 s⁻¹), and d) Real time on-off response test of ER fluids.

Figure 45. Optical microscope images of practical fibril-like structure formation of (a) W-HNP- and (b) S-HNP-based ER fluids under applied E field strength of 1.0 kV mm⁻¹.

List of Tables

- Table 1.** Summary of the characteristics of the WSNs according to all experimental conditions in the manuscript.
- Table 2.** Summary of MRR and surface roughness of the substrates before and after CMP.
- Table 3.** Summary of BET analysis of the silica spheres and WSNs with various sizes.
- Table 4.** Summary of Photovoltaic properties of WSNs and silica spheres-based DSSCs.
- Table 6.** Summary of BET analysis of WSNs, Spheres, and their derivatives.
- Table 7.** Dielectric properties of SiO₂ sphere and WSN-derived materials.

Table of Contents

Abstract	i
List of Abbreviations	iii
List of Figures	ix
List of Tables	xvi
List of Contents	xvii
1. Introduction	1
1.1. Background	1
1.1.1. Nanostructured Materials	1
1.1.1.1. Nanomaterials	1
1.1.1.2. Silica Nanomaterials	2
1.1.1.3. Mesoporous Silica Nanomaterials	7
1.1.1.4. Spherical Mesoporous Silica Nanomaterials	8
1.1.2. Applications	12
1.1.2.1. Chemical Mechanical Planarization	12

1.1.2.2. Dye Sensitized Solar Cells	14
1.1.2.3. Electrorheological Fluids	17
1.2. Objectives and Outlines	18
1.2.1. Objectives	18
1.2.2. Outlines.....	18
2. Experimental Details	22
2.1. Fabrication of Uniform Hierarchical Mesoporous Wrinkled Silica Nanoparticles	22
2.1.1. Fabrication of uniform hierarchical mesoporous wrinkled silica nanoparticles (WSNs)	22
2.1.2. Characterization of hierarchical mesoporous wrinkled silica nanoparticles	23
2.1.3. The chemical mechanical polishing performance evaluation of the WSNs as slurry abrasives	23
2.1.4. Performance of dye sensitized solar cells with scattering layer of WSNs	24

2.2. Fabrication of Hierarchical Mesoporous Wrinkled Silica Nanoparticle based-SiO₂/TiO₂ Hollow Nanoparticles	26
2.2.1. Fabrication of hierarchical mesoporous wrinkled silica nanoparticle based-SiO₂/TiO₂ hollow nanoparticles	26
2.2.2. Characterization of hierarchical mesoporous wrinkled silica nanoparticle based-SiO₂/TiO₂ hollow nanoparticles	27
2.2.3. Electrorheological properties of electrorheological fluid based on hierarchical mesoporous wrinkled silica nanoparticle based-SiO₂/TiO₂ hollow nanoparticles	27
3. Results and Discusions.....	29
3.1. Fabrication of Uniform Hierarchical Mesoporous Wrinkled Silica Nanoparticles	29
3.1.1. Fabrication of uniform hierarchical mesoporous wrinkled silica nanoparticles (WSNs)	29
3.1.2. Characterization of hierarchical mesoporous wrinkled silica nanoparticles	39
3.1.3. The chemical mechanical polishing performance evaluation of the WSNs as slurry abrasives	57

3.1.4. Performance of dye sensitized solar cells with scattering layer of WSNs	65
3.2. Fabrication of Hierarchical Mesoporous Wrinkled Silica Nanoparticle based-SiO ₂ /TiO ₂ Hollow Nanoparticles	80
3.2.1. Fabrication of hierarchical mesoporous wrinkled silica nanoparticle based-SiO ₂ /TiO ₂ hollow nanoparticles	80
3.2.2. Characterization of hierarchical mesoporous wrinkled silica nanoparticle based-SiO ₂ /TiO ₂ hollow nanoparticles	83
3.2.3. Electrorheological properties of electrorheological fluid based on hierarchical mesoporous wrinkled silica nanoparticle based-SiO ₂ /TiO ₂ hollow nanoparticles	98
4. Conclusion	112
Reference	115
국문초록.....	123

1. Introduction

1.1 Background

1.1.1. Nanostructured Nanomaterials

1.1.1.1. Nanomaterials

Nanomaterials have received much attention in the fields of chemistry, physics, biology, and engineering.[1, 2] The fabrication and application of nanomaterials with various unique properties has contributed to a huge leap over the past century in technological development in a variety of fields such as energy, industry, environment, electronics, cosmetics and medicine.[3, 4] Nanomaterials generally refer to materials smaller than one micrometer. One of the most important features of nanomaterials is the considerably larger surface area to volume ratio values than bulk materials. The smaller the size of the material, especially in the nano-range, the surface area to volume ratio exponentially increases.[5] In addition, a large number of specific atoms distributed on a wide surface or interface of nanomaterials have facilitated contact with other materials, and thus, there have been many reports on applications to catalysts, adsorbents, and abrasives, and fabrication of

composites with other materials.[6, 7]

Nanomaterials have been manufactured in various dimensions to meet the needs of specific fields, and various fabrication methods have been reported.[8-10] Furthermore, the size and morphology of nanomaterials have a significant impact on their physical and chemical properties, which affect the performance of the application.[11, 12] Therefore, size control and morphology change of nanomaterials is a strong requirement for advanced nanomaterial fabrication technology, and various methods have been suggested. However, despite the progress in nanomaterial fabrication and development of various shapes and morphologies, the manufactured materials exhibit a size distribution. The size uniformity of nanomaterials is closely related to a more detailed investigation of its size change and the reproducibility of fabrication. This, in turn, has a significant impact on industrial applications.

1.1.1.2. Silica Nanomaterials

Silicon dioxide, namely silica, is an oxide material of silicon, and its chemical formula is SiO_2 . This material is a substance commonly found in sand and quartz, and it is one of the abundant materials on

earth.[13] Silica is a component contained in most glass, and has become a very useful material in modern society. Nowadays, the nanotechnology applied to these silica materials has given a lot of interest to researchers in various fields such as catalyst supporters, adsorption, separation, drug delivery, electrodes, and hard templates, and its use has been broadened.[14-16] Silica nanomaterials can easily control their size and shape. In addition, they exhibit the features of easy surface modification, biocompatibility, hydrophilic surface, facile silane chemistry for surface functionalization, and low cost. Therefore, silica nanomaterials are not limited in their use and have led development especially in the field of *in vivo* applications.[17]

Colloidal silica is one of the most widely used types of silica nanotechnology.[18, 19] Due to many advantages such as high surface area, low toxicity, chemical and thermal stability, they have been used in applications such as support, drug carriers, and antifouling coating. The synthetic method of colloidal silica can be classified into two types, gaseous route and liquid route, and there are advantages and disadvantages of each.[20] **Figure 1** presents the various routes of chemical fabrication of colloidal silica. Among them, the microemulsion synthesis method has an advantage in fabricating

uniform silica nanoparticles.

Microemulsion is thermodynamically stable dispersions of two or more immiscible phases consisting of surfactant, water and oil, and the phase regions of the microemulsion system are displayed in **Figure 2**.^[21, 22] The added surfactant for stabilization of emulsion assembles at the interface of the droplet and the continuous phase, forming the micelle, and its size and shape can be controlled through the concentration adjustment.^[23] The microemulsion method can control the size, shape, and porosity of silica nanoparticles and is easy to fabricate mesoporous silica nanomaterials. The mesoporous silica nanomaterials are the most popular silica nanomaterials, and there have been many reports on various fabrication and application of them.

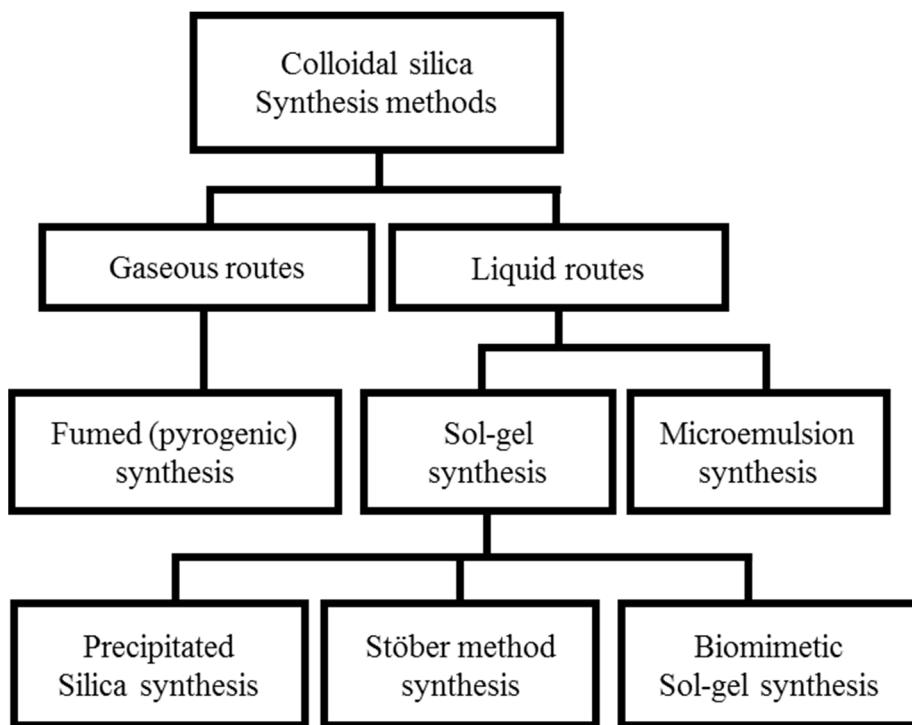


Figure 1. Routes of chemical fabrication of colloidal silica.[20]

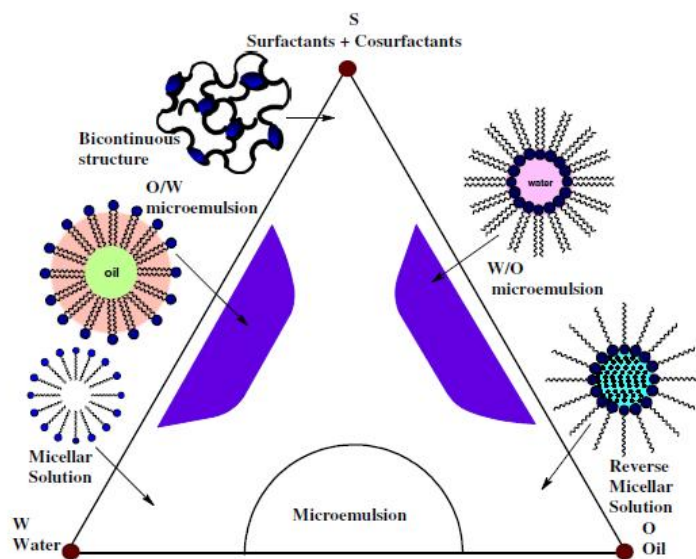


Figure 2. Phase regions of microemulsion systems.[21]

1.1.1.3. Mesoporous Silica Nanomaterials

Since the synthesis of MCM-41, mesoporous silica has received much attention.[24] ‘Mesoporous’ materials usually refer to materials with pores of 2 to 50 nm.[25] These structures with pores have been used extensively in a variety of applications such as catalyst supporter, adsorption, separation, drug delivery, electrodes, and hard templates due to unique features such as high surface area, high pore volume, and ordered pore structure.[26-28] The particle size and pore size of the mesoporous silica materials affect their physical and chemical properties. Therefore, controlling particle size, pore size, and morphology are important part of mesoporous silica material research.

The development of the soft template method using surfactant has been widely used to fabricate mesoporous silica with high surface area, high pore volume and tunable pore size.[29] The soft template method can control meso-structures, morphologies, and dimensions of mesoporous silica prepared using liquid crystal meso-phase and morphology of surfactant assemblies. This achievement was made possible by the study of the interaction between the surfactant and the silica precursor. Spontaneous assemble between surfactant and silica is approached with thermodynamic kinetics, and thus, it is possible to

control size, meso-structure, morphologies, etc. by carefully controlling parameters such as self-assembly and silica condensation rate. As a result, there has been reported a lot about the fabrication of application of mesoporous silica with various structures.[29-31]

1.1.1.4. Spherical Mesoporous Silica Nanomaterials

Among various structures of mesoporous silica,[32] spherical mesoporous silica nanoparticles have been attracting much attention because they provide excellent pore accessibility and smooth molecular diffusion.[29] The properties of spherical mesoporous silica nanoparticles have contributed to the development of such fields as packing materials for chromatography, drug delivery, cosmetics, and adsorption.[33, 34] Since size and morphology of the particles affect the physical and chemical properties of particles, the necessary investigation have conducted to regulate them.[35] Therefore, various methods for the fabrication of spherical mesoporous silica nanoparticle swith various type of pore structures have been attempted.[36-39]

Recently, hierarchical mesoporous wrinkled silica nanoparticles (WSNs) have been newly produced and they have attracted great

interests as materials for chromatography, surface polishing, medical implants, catalysts and drug delivery.[38, 40] These small sized silica with wrinkled structure exhibited high surface-to-volume ratio and high dispersity in various solvent as a colloidal solution. Furthermore, the high accessibility of WSN to guest material had been expected to be highly utilized in various fields.

The wrinkled structure of WSNs was formed by bicontinuous microemulsion phase in Winsor III system, and the inter-wrinkle distance of WSN could be easily adjusted by controlling the behavior of microemulsion phase.[39, 41] Winsor system refers to ternary systems of water, oil, and surfactant at low surfactant concentrations, which were investigated by researchers including Winsor.[42] The Winsor system showed four types of phase behavior as schematically represented in **Figure 3**, which is determined by surfactant concentration, surfactant type, and component ratio of the compositions. The Winsor III system represents the equilibrium state of three-phase system consisting of oil in the upper layer, water in the lower layer, and bicontinuous microemulsion consisting of most of the surfactant along with similar amounts of water and oil in the middle layer.[43] In this dissertation, uniform WSNs were fabricated using the bicontinuous

microemulsion phase of the Winsor III system. Furthermore, the superiority of spherical mesoporous silica nanoparticles was demonstrated by applying the prepared WSNs to abrasives in chemical mechanical planarization, light scattering materials in dye sensitized-solar cell, and Electrorheological fluids.

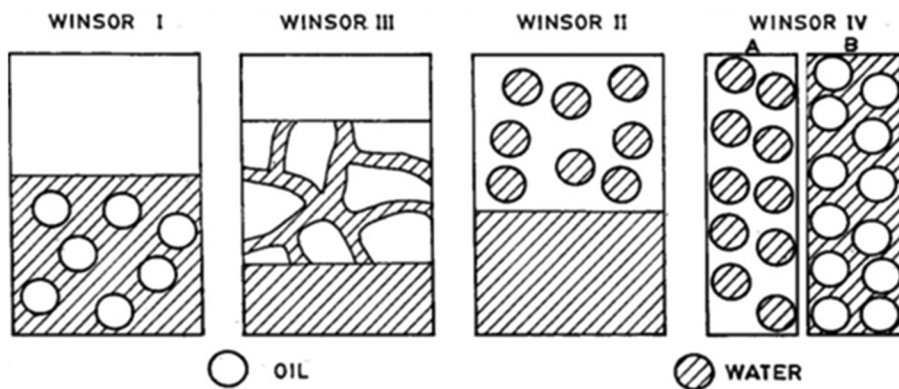


Figure 3. Schematic representation of four type of Winsor system.[44]

1.1.2. Application Fields

1.1.2.1. Chemical Mechanical Planarization

Chemical mechanical planarization (CMP) is a process of planarizing the surface of a wafer using a combination of chemical corrosion and mechanical polishing, which is a process involved in the semiconductor manufacturing process.[45] The CMP process was illustrated in the **Figure 4**. In a typical CMP process, a wafer is pressed down against a polishing pad. As the wafer and pad rotate, the surface of the wafer is smoothly polished by the slurry flowing into the interface between the wafer and the pad.[46]

There has been a demand for miniaturization of wiring patterns due to high integration of semiconductor devices.[47] In addition, the homogeneity of the surface to be polished has become more remarkable in addition to the purpose of simple planarization. Therefore, the studies of slurry conditions including abrasive materials and additives have been focused. Recently, mesoporous nanoparticles of low hardness (H) and Young's modulus (E) has been shown to contribute to improving the CMP performance, and researches using mesoporous nanoparticles as abrasive materials have attracted attention.[48, 49]

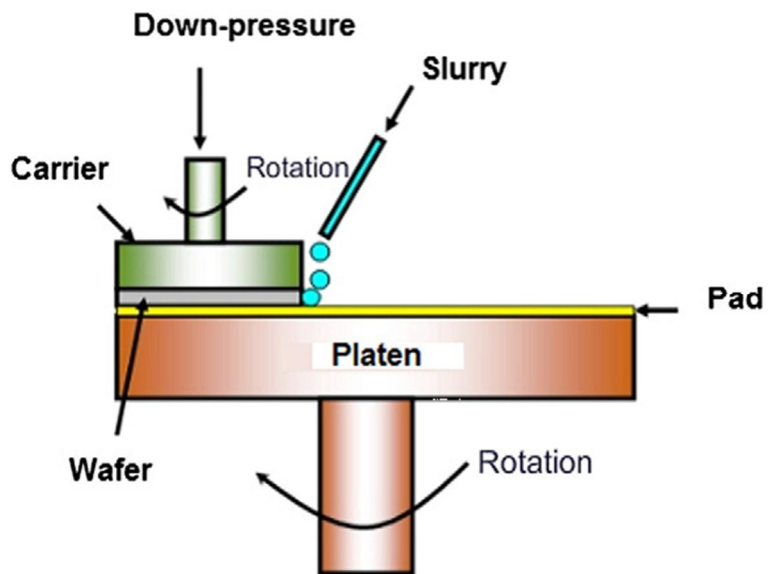


Figure 4. Schematic illustration of CMP process.[50]

1.1.2.2. Dye Sensitized Solar Cells

Dye-sensitized solar cells (DSSCs) are photovoltaic devices characterized by relatively high efficiency and low manufacturing costs.[51] The structure and operating mechanism of the DSSCs were shown in **Figure 5**. Dye as photo-sensitizer absorbs light to generate electron-hole pairs and the photo-excited electrons were injected into the conduction band of metal oxide. From this viewpoint, the light absorption capacity of photoanode plays an important role in photo-excited electron generation, which is directly related to the high efficiency of the device. Therefore, many researchers have made various attempts to improve light harvesting, such as the modification of metal oxide structures and the development of new dyes.[52-54]

The light scattering strategy is also one of the optimal absorption enhancements of photoanode. The light scattering capability of the anode extends the traveling distance of light within the anode, which further enhances interaction with the dye.[55] Hierarchical nanomaterials have recently attracted a great deal of interest in terms of overcoming the demerits of conventional methods, which use large particles for light scattering in DSSCs.[56] This highly porous material, which shows large surface area in spite of the large diameter,

provides both light scattering effect and increase in dye loading amount. For these reasons, many studies have focused on the fabrication of hierarchical-structured metal oxide nanomaterials, and applying them in DSSCs as a scattering layer.[57, 58]

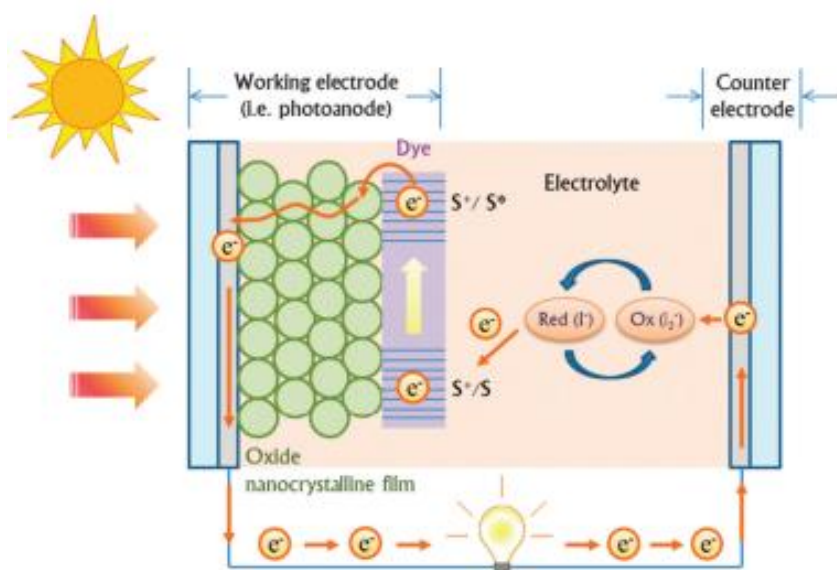


Figure 5. Structure and operating mechanism of a dye sensitized solar cell.[59]

1.1.2.3. Electrorheological Fluids

Electrorheological (ER) fluids, consisting of electrically polarizable particles as dispersed phase and insulating oil as dispersing phase, are smart materials that can control the rheological properties such as viscosity, shear modulus, yield stress, and reversible change of structure under applied voltage to create an external electric field.[60] When an electrical field is applied to a fluid, it forms a fibrous structure parallel to the electrical field, while at the same time exhibiting the properties of a solid-like material.[61] That is, the ER effect can be changed from a fluid-like material to a solid-like material within a millisecond under an electrical field. Therefore, the ER fluids have great potential to be applied in various fields such as robotics, automobiles, and military industry.[62] However, the main problem of the ER fluids is sedimentation of particles, which hinders commercialization of ER fluids. To solve the problem, various attempts have been made through chemical and structural modification of particles.[63, 64] Among the many attempts, the introduction of hollow structured-materials with low density into the ER fluid has attracted much attention in solving the sedimentation problem.[65, 66]

1.2. Objectives and Outlines

1.2.1. Objectives

The aim of this dissertation is to describe a method for fabricating uniform hierarchical mesoporous wrinkled silica nanoparticles using the bicontinuous microemulsion phase of the Winsor III system. Furthermore, a complete method for high-yield production of uniform WSNs with tunable particle size and pore size is proposed by investigating factors affecting the particle size and pore size of the WSNs. The prepared WSNs are applied to slurry abrasives in CMP, scattering layer in DSSCs, and hard template for the fabrication of nanocomposite used as material in ER fluid. Finally, the superiority of spherical mesoporous silica nanoparticles is verified by comparing the performance of each application of WSNs with that of non-porous silica spheres of the same size.

1.2.2. Outlines

This dissertation focused on the fabrication of monodispersed-WSNs and its applications. In viewpoint of prepared WSNs and application field, this dissertation involves the following subtopics;

- I. Uniform hierarchical mesoporous wrinkled silica nanoparticles for abrasives in Chemical Mechanical Planarization

- II. Uniform hierarchical mesoporous wrinkled silica nanoparticles for light scattering material in dye sensitized solar cells
- III. Hierarchical mesoporous wrinkled silica nanoparticles based-SiO₂/TiO₂ hollow nanoparticles for electrorheological fluid

A detailed outline of the study is as follows:

1. Monodispersed-hierarchical mesoporous wrinkled silica nanoparticles (WSNs) were fabricated using bicontinuous microemulsion phase in Winsor III system. Cooling the reactants at the appropriate moment during the reaction allowed complete separation of the nucleation and growth stages, resulting in uniform WSN fabrication. Additionally, controlling factors such as the temperature, the oil-to-water ratio of the reaction mixture, and the amount of co-solvent, the size and pore size of the WSNs were investigated. This method could produce uniform WSNs with various sizes and pore sizes, with high yield. The fabricated 100-nm-sized WSNs were used as CMP slurry abrasive materials. The results indicated that the mesoporous structure of the WSNs resulted in higher CMP performance, compared with non-porous silica spheres of

the same size and a fumed silica-based commercial product under same condition.

2. Uniform hierarchical mesoporous wrinkled silica nanoparticles (WSNs) with various sizes were applied in DSSCs as a scattering layer. It is valuable in that it was the first attempt to apply hierarchical silica nanoparticles in DSSCs device. Furthermore, a study on how surface morphology of spherical particles affects light scattering effect was investigated through a comparison in WSNs and non-porous SiO₂ nanospheres of the same size. Importantly, the results demonstrated that WSNs stand out as outstanding light scattering material, which provides multiple light scattering by numerous SiO₂ / air (electrolyte) interface.

3. Hierarchical mesoporous wrinkled silica nanoparticles (WSNs) was used as a hard template to fabricate WSN based-SiO₂/TiO₂ core/shell nanoparticles (W-STCSs) and WSN based-SiO₂/TiO₂ hollow nanoparticles (W-HNPs), and the electrorheological (ER) performance of each material was evaluated. Especially, the inner surface of the W-HNP shell reflected a unique structure in which the hierarchical

structure of WSNs was maintained. This unique structure represented a distinct difference from the morphology of SiO_2 sphere based- $\text{SiO}_2/\text{TiO}_2$ hollow nanoparticles (S-HNPs) prepared using SiO_2 sphere to investigate the morphological effect of ER performance, which contributed to higher surface area than S-HNPs. Furthermore, W-HNP manifested improved ER performance over S-HNP by their unique morphology, demonstrating that it was a promising material of ER fluid.

2. Experimental Details

2.1. Fabrication of Uniform Hierarchical Mesoporous Wrinkled Silica Nanoparticles

2.1.1. Fabrication of uniform hierarchical mesoporous wrinkled silica nanoparticles (WSNs)

2 g (5.2 mmol) of cetylpyridinium bromide and 1.2 g (20.0 mmol) of urea were dissolved in 60 mL of water. And then, 30 mL of cyclohexane and 1.84 mL (24 mmol) of iso-propanol were added to the solution. With vigorous stirring, 5 g (24 mmol) of TEOS was dropwised to the mixed solution. After vigorous stirring for 30 min at room temperature, the reaction was proceeded at 70 °C for 1h. After the reaction, the reator was immediately transfer to the water bath for the cooling precess at 10 °C for 2 h. Then, the reaction at 70 °C was resumed, and this state was maintained for 12 h. The reaction mixture washed with ethanol 3 times through centrifugation. The isolated WSNs by centrifugation were dried in the 70 °C. Finally, the dried WSNs were calcined at 550 °C for six hours in air.

2.1.2. Characterization of hierarchical mesoporous wrinkled silica nanoparticles

The size of WSNs was confirmed by using transmission electronic microscopy (TEM) images. The surface morphology of WSNs was confirmed by using scanning electronic microscopy (SEM) images. Surface area and pore size of the WSNs were measured using Brunauer Emmett Teller (BET) analysis.

2.1.3. The chemical mechanical polishing performance evaluation of the WSNs as slurry abrasives

Si coupon wafers ($2.0\text{ cm} \times 2.0\text{ cm}$) were used for the estimation of the effectiveness of each kind of abrasive. The Si coupon wafers prepared by thermal Si oxide (1050 nm) and Si substrate. The Oxide CMP slurry included 1wt% colloidal silica (100 nm). The pH of solution was fixed at 10 by adding potassium hydroxide (KOH). To meet the target layer, pH 10 was chosen. Si coupon wafers were polished using a CMP planarizer (POLI-400, G&P Tech. inc., Korea) with an industrial standard CMP pad (IC 1000/Suba IV, Rohm and Haas Electronic Materials, U.S.A). After CMP, the wafers were cleaned using an ammonia peroxide mixture solution

($\text{NH}_4\text{OH}:\text{H}_2\text{O}_2:\text{H}_2\text{O} = 1:1:10$) at 80 °C to eliminate residual particles.

2.1.4. Performance of dye sensitized solar cells with scattering layer of WSNs

A double-layered structure of the TiO_2 film was composed of the TiO_2 -NP (Solaronix, Ti-Nanoxide T/sp) underlayer and the WSNs with TiO_2 NPs overlayer as a scattering layer. To prepare a mixture of WSNs and paste, the WSNs were added to the paste which mixture of lauric acid, ethyl cellulose, and terpineol containing TiO_2 NPs (size = 15 - 20 nm). Fluorine-doped tin dioxide (FTO) glass substrates were cleaned by successive sonication in deionized water, acetone, and 2-propanol for 60 min each, and then treated with oxygen plasma for 30 s. The FTO glass substrate was pretreated with an aqueous solution of TiCl_4 (40 mm) and heated at 450 °C for 30 min. The double-layered structure of the TiO_2 film which composed of TiO_2 -NP under-layer and WSNs with TiO_2 NPs over-layer was prepared by using a screen print onto the FTO substrate. The TiO_2 films were sintered at 450 °C for 30 min, and then treated with TiCl_4 and sintered again as above. The resulting TiO_2 films were immersed in absolute ethanol containing N719 dye (5×10^{-4} M) and kept at room temperature for 24

h. Pt counter electrodes were prepared on the FTO glasses using a 2-propanol solution of H_2PtCl_6 (5 mM), followed by heating at 400 °C for 30 min in air. The electrolyte in the sealed cell was an $\text{I}^- / \text{I}^{3-}$ redox couple containing BMII (0.60 M), LiI (0.1 M), I₂ (0.05 M), and tert-butylpyridine (0.5 M) in acetonitrile. Measurements were performed under AM 1.5 G one sun light intensity of 100 W cm⁻² and the active areas were about 0.16 cm² for all of the cells.

2.2. Fabrication of Hierarchical Mesoporous Wrinkled Silica Nanoparticle based-SiO₂/TiO₂ Hollow Nanoparticles

2.2.1. Fabrication of hierarchical mesoporous wrinkled silica nanoparticle based-SiO₂/TiO₂ hollow nanoparticles

1.0 g of WSNs was dispersed in the mixed solution with 79 mL of ethanol, 3.9 mL of ammonia, and 1.4 mL of water. Then, 28 mL of acetonitrile was added to the WSN colloidal solution with stirring at 4°C. Another solution containing 36 mL of ethanol, 12 mL of acetonitrile, and 4.6 mL of titanium(IV) isopropoxide (TTIP) was prepared followed by dropwise addition to the colloidal solution. The mixture was maintained with vigorous stirring for 12 h. The fabricated W-STCS were obtained by centrifugation at 12,000 rpm for 20 min. The hollow structure was fabricated by re-deposition in a 0.1 M ammonia solution and sonication-mediated etching for 6 h. The final W-HNP product was obtained by centrifugation at 12 000 rpm for 10 min and washing the solution with ethanol twice. The isolated H-HNPs by centrifugation were dried in the 70 °C.

2.2.2. Characterization of hierarchical mesoporous wrinkled silica nanoparticle based-SiO₂/TiO₂ hollow nanoparticles

Images of transmission electron microscopy (TEM) were obtained from LIBRA 120 (Carl Zeiss, Germany). FE-SEM images were obtained from JSM-7800F Prime (JEOL Ltd, Japan). Brunauer–Emmett–Teller (BET) surface areas were measured using a Micromeritics analyzer (ASAP 2000; Micromeritics Co., Norcross, GA). The electron energy loss spectroscopy mapping and scanning transmission electron microscopy-energy dispersive spectroscopy (STEM-EDS) line analyses were performed using a JEOL JEM-2100F instrument.

2.2.3. Electrorheological properties of electrorheological fluid based on hierarchical mesoporous wrinkled silica nanoparticle based-SiO₂/TiO₂ hollow nanoparticles

All ER fluids were formulated according to the following procedures. Firstly, particles were dried in oven (90 °C) for overnight to completely remove the moistures. Dried particles (0.3 g) were ground by mortar and pestle and dispersed into silicone oil (11.0 mL, viscosity = 100 cSt). For complete dispersion, as-prepared ER fluids

were vigorously stirred using a magnetic stirrer for 24 h. Also, no additive other than particles and silicone oil were added to the ER fluids. The ER activities of ER fluids were examined by rheometer (AR2000, TA instruments) with accessories of a container cup (d: 30.0 mm and h: 30.0 mm), concentric cylinder conical geometry (d: 28.0 mm and height: 30.0 mm), and voltage generator (Trek 677B). The gap distance of geometry and cup was set to 1.0 mm on each side (total: 2.0 mm) without contacting and friction between them. For practical ER measurements, well-dispersed ER fluids were added into the cup and geometry inserted. Prior to applying the E field, pre-shear of 10.0 s^{-1} was applied for 10 min to attain an equilibrium state of fluid. Finally, intended strength of E field and appropriate testing mode was selected to investigate ER properties of ER fluids.

3. Results and Discussions

3.1. Fabrication of Uniform Hierarchical Mesoporous Wrinkled Silica Nanoparticles

3.1.1. Fabrication of uniform hierarchical mesoporous wrinkled silica nanoparticles (WSNs)

Figure 6a and b shows transmission electron microscopy (TEM) images of WSNs prepared with and without the cooling process at 10 °C for 2 h, respectively. The reaction time at 70 °C of both samples was the same, at 7 h, and the time was counted from when the temperature reached 70°C. The cooling process was added for 2 h after the 1h reaction time, and then the reaction proceeded again at 70 °C for 6 h. The sizes of WSNs fabricated with and without the cooling process were 90 ± 5 nm and 150 ± 25 nm, respectively, as shown in **Figure 6c**. Although the same heating time was used for both reactions, the addition of the cooling process produced smaller and more uniform WSNs. The production of nanoparticles across a wide size distribution is mostly based on simultaneous nucleation and growth, and uncontrolled primary particle (or seed) aggregation.[29, 67, 68] Secondary particle formation during seed particle growth also

causes a broad size distribution.[69, 70] The cooling process could prevent the broad size distribution in nanoparticle production by suppressing these causes. The effect of the reaction time before the cooling process (hereafter referred to as the pre-reaction) was investigated in **Figure 7**. All samples had the same reaction time of 6 h at 70°C after the cooling process, given that the reaction after cooling (hereafter referred to as the post-reaction) was related to seed growth. The size and size distributions of the WSNs fabricated with 0 h and 0.5 h of pre-reaction were similar to those of the direct 7 h reaction without cooling, corresponding to **Figure 6b**. However, the cooling process after pre-reaction of 1 h and 2 h enabled fabrication of uniform reduced-size WSNs. This suggests that 1–2 h from the start of the reaction was an important timeframe in the fabrication of uniform WSNs. As such, we refer to this period as the burst nucleation stage. Uniform nanoparticles of about 20 nm in size, as primary particles (or seeds), were observed from the middle layer of the reaction system after 1h reaction, which formed a bicontinuous emulsion structure as illustrated in **Figure 8**. Rapid cooling of the reaction system during the nucleation stage stopped the formation and growth of primary particles. In addition, because stabilization of the particles could

reduce aggregation in the subsequent reaction, our results suggest that rapid cooling of the reactants stabilized the unstable primary particles.[71, 72] When the reaction was resumed, the particles stabilized in the cooling process proceeded to grow rather than form new particles, because this was more thermodynamically favorable.[73] Thus, rapid cooling initiated a mechanism similar to that of ‘seeded growth’.[41, 74, 75] For a 2 h pre-reaction, the WSNs were smaller (70 nm) than in the 1 h pre-reaction stage (90 nm), because more nuclei formed during the nucleation stage.[76] This indicates that TEOS was applied uniformly over all nuclei for growth. In addition, the WSNs fabricated with a 1 h pre-reaction at 80°C before cooling (6 h post-reaction) had a diameter of 70 nm, smaller than with the same pre-reaction time at 70°C as presented in **Figure 9**. It could therefore be inferred that the increased reaction temperature increased the hydrolysis rate of TEOS, leading to the formation of more seeds than the reaction at 70°C.[77] Furthermore, our results reflect that particle formation dominated during the nucleation stage. **Figure 10** reveals the particle distribution of the WSNs fabricated when the cooling process was applied after the first 3 h of heating at 70°C. This indicates that disordered aggregation and rapid growth of

the formed nuclei proceeded after around 3 h into the reaction, and the cooling process had no effect at this stage. Based on these results, a WSN formation mechanism with the added cooling process was proposed, as manifested in **Figure 11**. A pre-reaction of 1 h at 70°C before the cooling process (at 10°C for 2 h) was set as the basic condition for WSN fabrication, for further investigation.

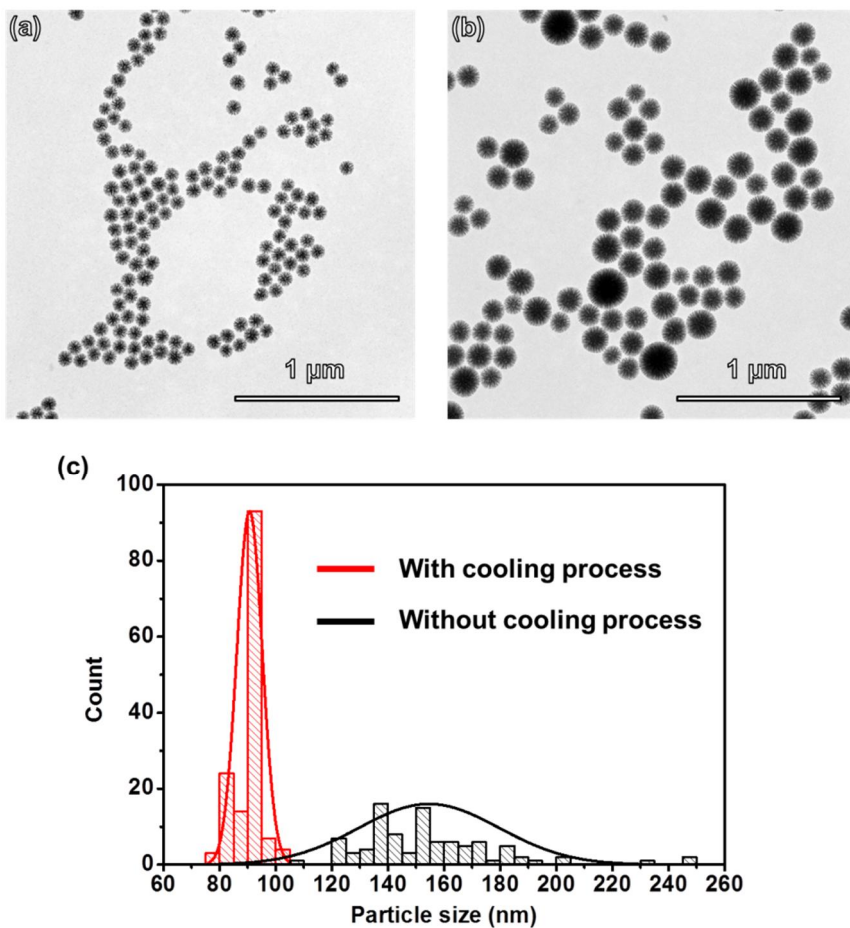


Figure 6. TEM images of WSNs fabricated (a) with and (b) without cooling process. (c) Size distribution profiles of WSNs fabricated with and without cooling process.

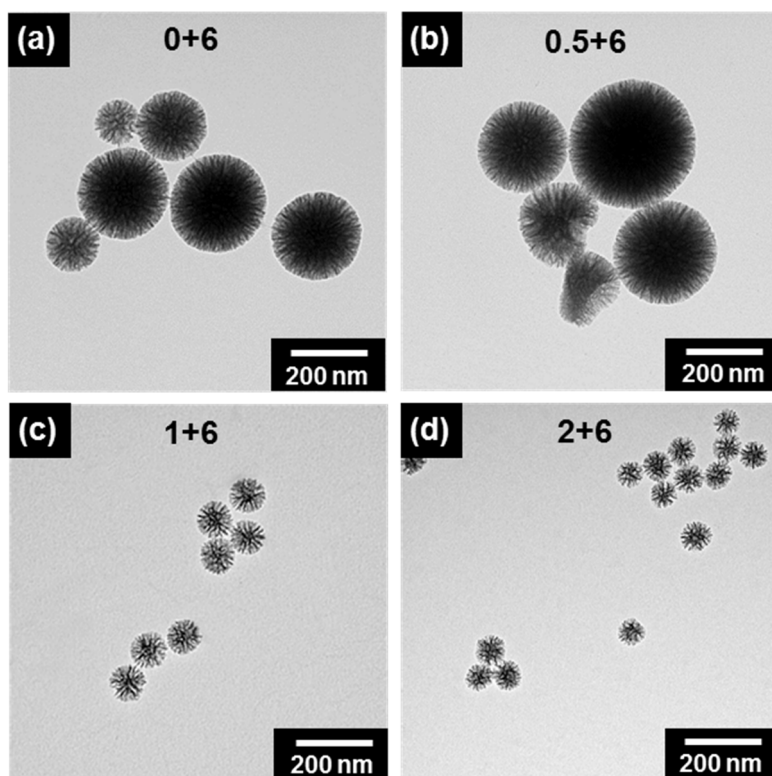


Figure 7. TEM images of the WSNs reacted at 70 °C for (a) 0, (b) 0.5, (c) 1, and (d) 2 h before cooling process. The reactions of all samples proceed for 6 h at 70 °C after cooling process.

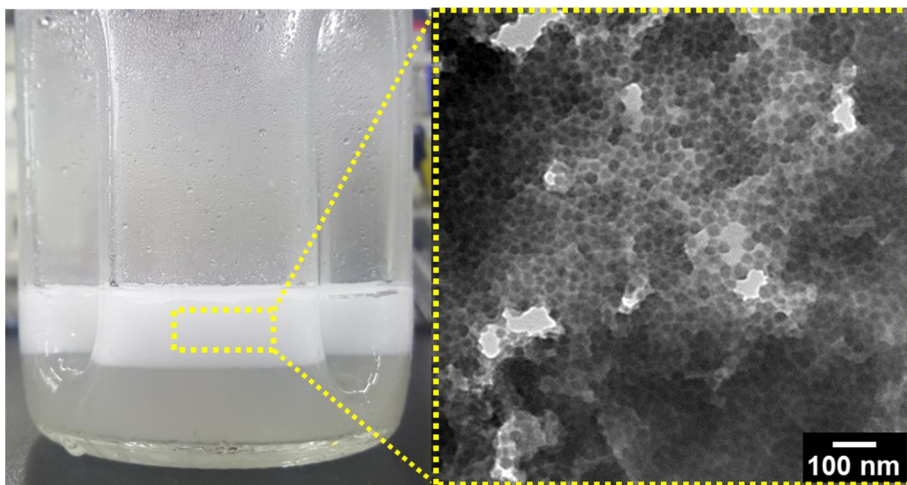


Figure 8. The photo picture of the reaction mixtures after cooling process and TEM images of primary particles of WSN.

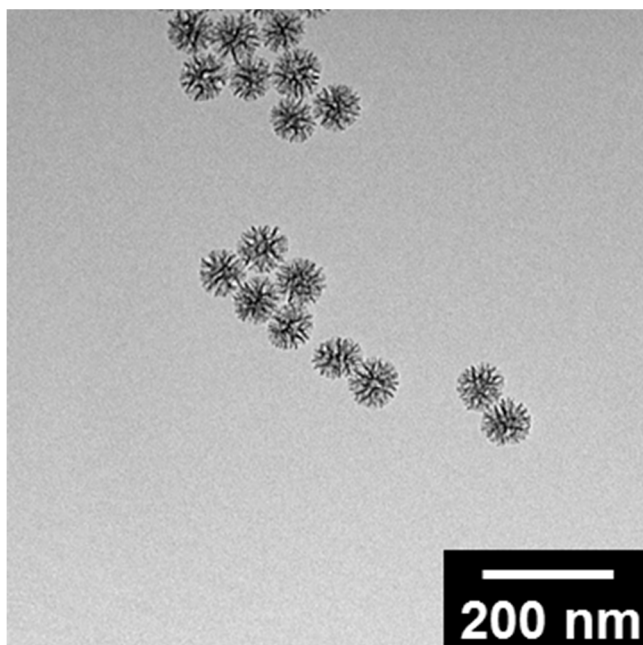


Figure 9. TEM image of the WSNs reacted at 80 °C for 1 h before cooling process. After cooling process, the reaction proceeded for 6 h at 70 °C.

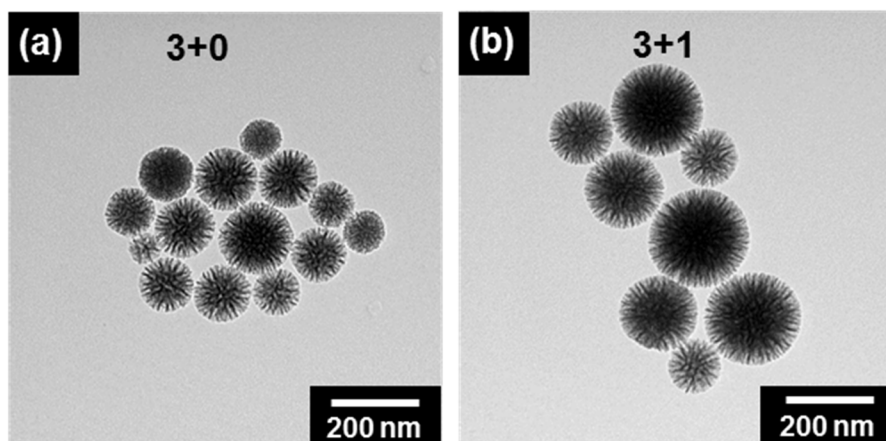


Figure 10. TEM images of WSNs fabricated at 70 °C for (a) 3 h without cooling process and (b) 3 h before cooling, followed by 1 h.

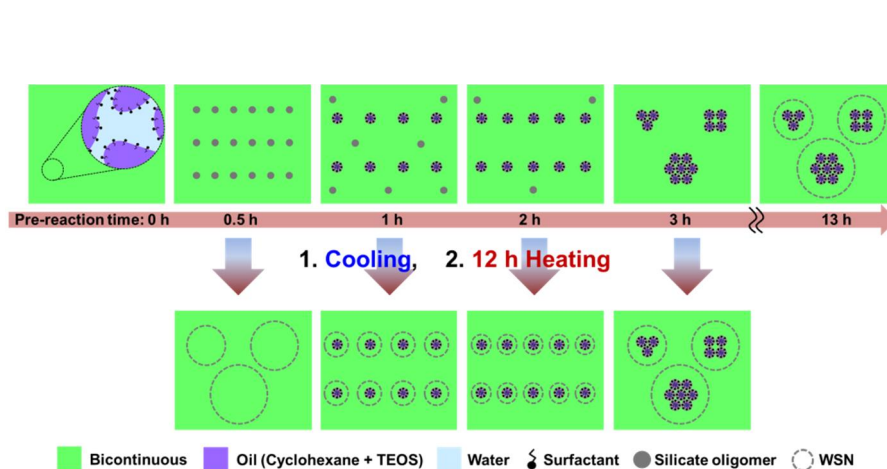


Figure 11. Proposed the uniform WSN forming mechanism with the added cooling process during the reaction.

3.1.2. Characterization of hierarchical mesoporous wrinkled silica nanoparticles

The effect of the reaction time after the cooling process (post-reaction) was investigated. **Figure 12** exhibited TEM images of WSNs with various post-reaction times after a 1 h pre-reaction and the cooling process. All reactions proceeded at 70 °C. WSNs of various sizes, 50, 65, 90, and 100 nm were fabricated with post-reaction times of 2, 3, 6, and 12 h, respectively, and the pore size was unchanged.[78] In other words, the size of the WSNs increased with the post-reaction time; however, the size growth rate of the WSNs decreased with time. **Figure 13** represented that the particles did not grow further after 12 h of post-reaction time.[78] The decrease in growth rate with subsequent reaction time was due to the pH change of the reaction mixture with urea, which was the base catalyst. The pH of the mixture changed from 7 at the beginning of the reaction to 10 after a total of 13 h of heating time, through the thermal decomposition of urea. The yield of the fabricated WSNs was also investigated for a range of post-reaction times. The variation in WSN yield showed a similar tendency to that of size growth. After 12 h of post-reaction, the relative ratio of WSNs at 70 °C to TEOS addition, as a silica precursor, was about 28.4%,

comparable to the yield of the Stöber method.[79] Because a post-reaction time of more than 12 h provided a high WSN yield, a 12 h post-reaction time was set as the basic experimental condition for further investigation of WSN sizes and pore sizes.

The sizes of WSNs and their inter-wrinkle distance (= pore size) were investigated for a range of reaction temperatures. All experiments were carried out with various temperatures of 12 h post-reaction after 1 h pre-reaction at 70 °C and the cooling process. **Figure 14** shows TEM and scanning electron microscopy (SEM) images and Barrett–Joyner–Halenda (BJH) pore distribution plots of WSNs prepared using 70, 75, and 80 °C post-reactions, respectively. WSNs could not be obtained with a post-reaction at 60 °C. The size of WSNs increased with increasing post-reaction temperature;[75, 80, 81] this was attributed to the increased condensation rate of silicic acid at higher temperatures.[82] In contrast, both samples exhibited the same peaks in the BJH plot, at about 3 nm (corresponding to the pores of the core portion) and 15 nm (corresponding to the inter-wrinkle distance). This indicates that the temperature affected the size of the WSNs but did not affect the morphology. The WSNs could be grown through a bicontinuous template under typical reaction conditions with

a fixed average distance between the layers.[39] N₂ adsorption–desorption isotherms were used for Brunauer–Emmett–Teller (BET) surface area measurements, as exhibited in **Figure 15**. The isotherms showed IV- and H3-type hysteresis loops, indicating that the WSNs had mesoporous features with slit shapes.[83, 84] The BET surface area of WSNs prepared using a post-reaction at 80 °C (= 616.85 m²g⁻¹) was the highest, followed by those at 75 °C (= 583.09 m²g⁻¹) and 70 °C (= 533.36 m²g⁻¹). The surface area of WSNs of the same morphology tended to increase with increasing size. This was attributed to an increase in the 3-nm pore volume as the size of the WSNs increased, as shown in BJH plots. Pores of 3 nm size formed in the core portion of the WSNs; the increase in the WSN cores with increasing WSN size was confirmed by TEM images. In addition, as the size of the WSNs increased, especially above 200 nm, the shape of the N₂ isotherm changed gradually from a H3 hysteresis loop to a H1 hysteresis loop. These results were attributed to an increase in the core portion of the WSNs, with a core structure based on ordered three-dimensional pore networks.[83]

The size and morphology of the WSNs were investigated using the oil-to-water ratio of the reaction mixture. **Figure 16** revealed TEM

images and BJH plots of the WSNs fabricated in reaction mixtures with oil-to-water ratios of 0.5 and 1, respectively, under the same fabrication conditions. The sizes of the WSNs prepared in the reaction mixtures with an oil-to-water ratio of 0.5 and 1 were 100 nm and 250 nm, respectively, and the inter-wrinkle distances were about 15 nm and 21 nm, respectively. Both the size and the wrinkle distance increased as the oil-to-water ratio increased. As the amount of oil in the emulsion system increased, a swollen micelle formed, which increased the number of surfactant molecules required per micelle.[85] This reduced the number of seeds formed during the nucleation stage, and increased both the size and the pore size of the final fabricated WSNs. The surface area of the WSNs prepared in the reaction mixtures with oil-to-water ratios of 0.5 and 1 were 533.36 and 583.51 m^2g^{-1} , respectively (**Figure 17**).

The size of the WSNs was changed without morphology change by controlling the amount of added 2-propanol (iPA) co-solvent. **Figure 18** reflected TEM images and BJH plots of WSNs fabricated with different amounts of iPA; ‘*1 iPA’ denotes the addition of 1.84 mL iPA as the basic condition; ‘*0.5 iPA’ and ‘*1.5 iPA’ indicate the addition of 0.5 times and 1.5 times the basic amount of iPA,

respectively, corresponding to 0.92 mL and 2.76 mL. The WSN sizes of *0.5, *1, and *1.5 iPA were about 70, 100, and 200 nm, respectively, and the inter-wrinkle distance of the samples were all *ca.* 15 nm. The size of WSNs increased with the amount of iPA; however, the morphology of the WSNs remained stable. With increasing amounts of added co-solvent, the miscibility of the oil in the emulsion phase increased due to the hydrophobic alkyl chain. This resulted in an increase in WSN size. However, the pore size was maintained despite the increase in the amount of oil interacting with the micelle in the phase, due to an increase in the amount of co-solvent. Alkyl alcohol, as a co-solvent, exhibits amphiphilic properties, and in turn increased the water miscibility in the emulsion phase via the hydroxide group. The miscibility of the oil/water mixture, which affected micelles in the phase, remained constant with respect to the oil-to-water ratio. The amount of oil interacting with the micelle in the phase increased with increasing co-solvent amount; however, the miscibility of the oil/water mixture was constant regardless of the amount of co-solvent. This would result in a change in the size of the WSNs without changing the inter-wrinkle distance. In other words, based on these results, it can be concluded that the oil-to-water ratio of

the emulsion phase affects the inter-wrinkle distance of the formed WSNs, and the amount of oil interacting with the phase affects the size of the WSNs. The BET surface areas of the WSNs with the addition of *0.5, *1, and *1.5 iPA were 509.37, 533.36, and 575.25 m^2g^{-1} , respectively (**Figure 19**). WSNs with the same morphology tended to exhibit an increase in their surface area with increasing size, consistent with the previous results.

The co-solvent was replaced by 1-butanol to further confirm changes in the WSNs with different amounts of co-solvent. TEM and SEM images and BJH plots of the WSNs fabricated using iPA and 1-butanol as a co-solvent are shown in **Figure 20**. Compared with the use of iPA as co-solvent, WSNs prepared using the same molar amount of 1-butanol manifested an increased size (400 nm) and pore size (33 nm). 1-Butanol has a longer alkyl chain than iPA, which increased the hydrophobicity of the surfactant, thereby increasing the amount of interacting oil and also the oil-to-water ratio. In addition, 100-nm-size WSNs with the same inter-wrinkle distance (33 nm) were fabricated by reducing the amount of butanol added. This is consistent with the discussion above. The BET surface areas of the WSNs with *1 butanol, and *0.5 butanol were 572.36 and 514.35 m^2g^{-1} ,

respectively as represented in **Figure 21**. The characteristics of the WSNs prepared using the experimental conditions described above are summarized in **Table 1**.

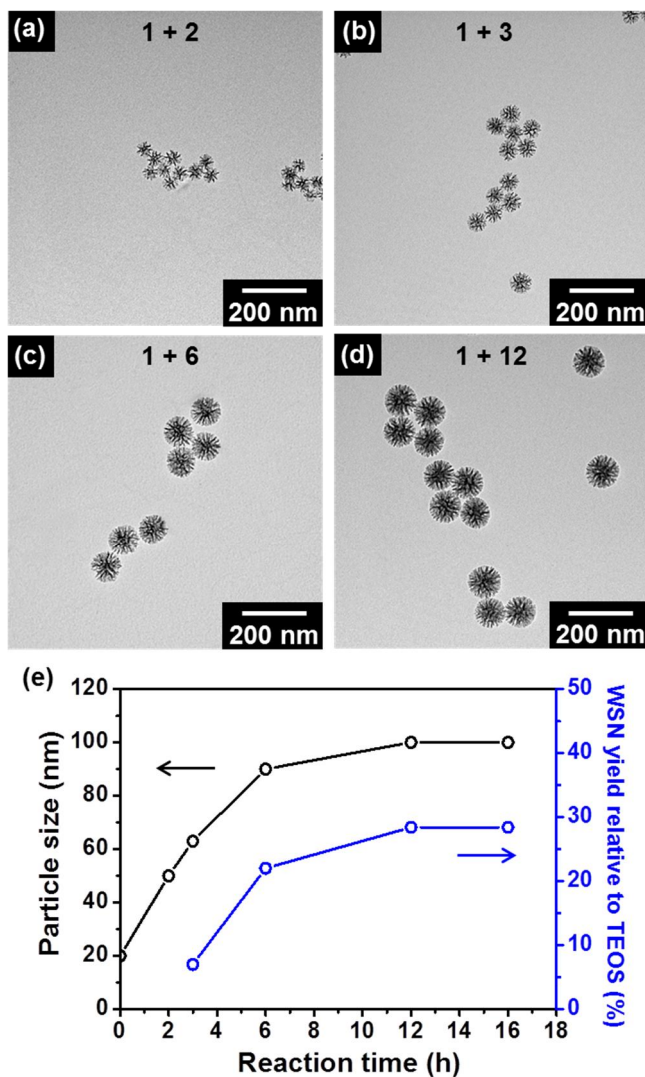


Figure 12. Effect of reaction time after cooling process; TEM images of the WSNs reacted at 70 °C for (a) 2 h, (b) 3 h, (c) 6 h, and (d) 12 h after 1 h pre-reaction and cooling process. All samples reacted before cooling process for 1 h at 70 °C. (e) Variation of WSN size and WSN yield relative to addition amount of TEOS as function of the reaction time.

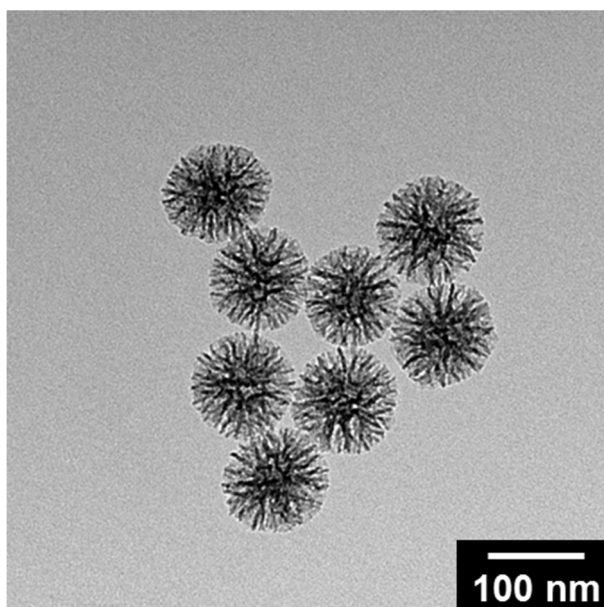


Figure 13. TEM image of the WSNs reacted at 70 °C for 16 h after 1 h pre-reaction and cooling process.

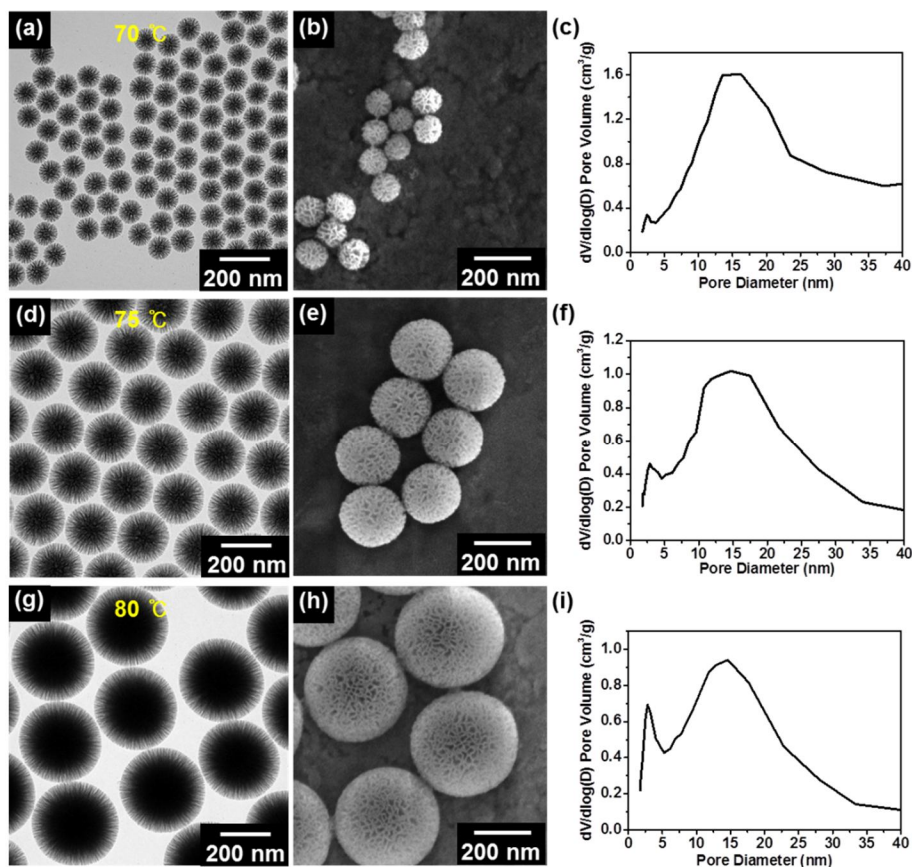


Figure 14. Effect of reaction temperature after cooling process; TEM images, SEM images and the corresponding BJH plots of the WSNs reacted at (a, b, c) 70, (d, e, f) 75 °C, and (g, h, i) 80 °C for 12 h after cooling process. All samples reacted before cooling process for 1 h at 70 °C.

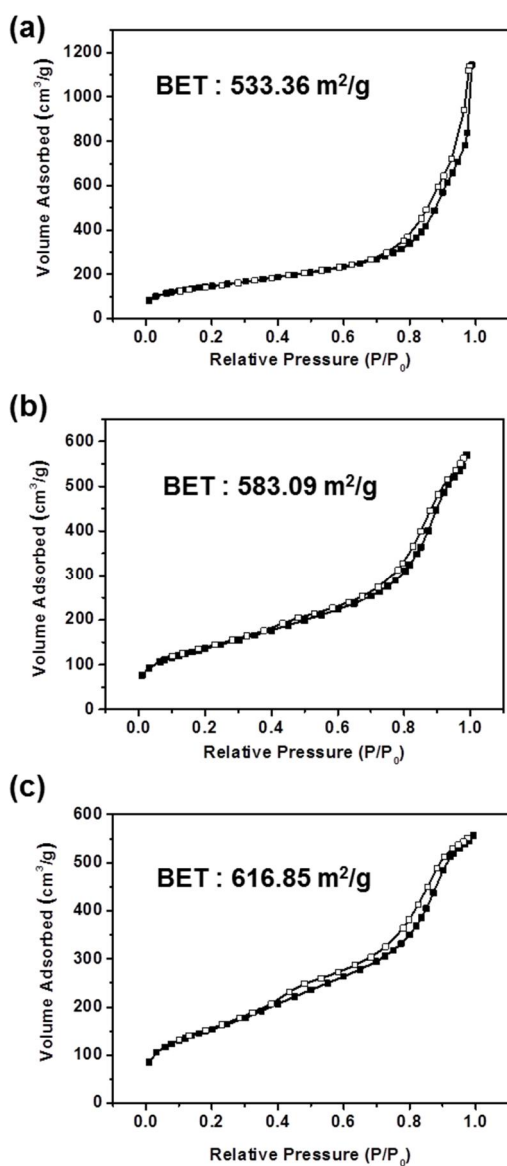


Figure 15. N_2 adsorption-desorption isotherms of the WSNs reacted at (a) 70, (b) 75, and (c) 80 $^\circ\text{C}$ for 12 h after cooling process. All samples reacted before cooling process for 1 hour at 70 $^\circ\text{C}$ (corresponding with **Figure. 3**).

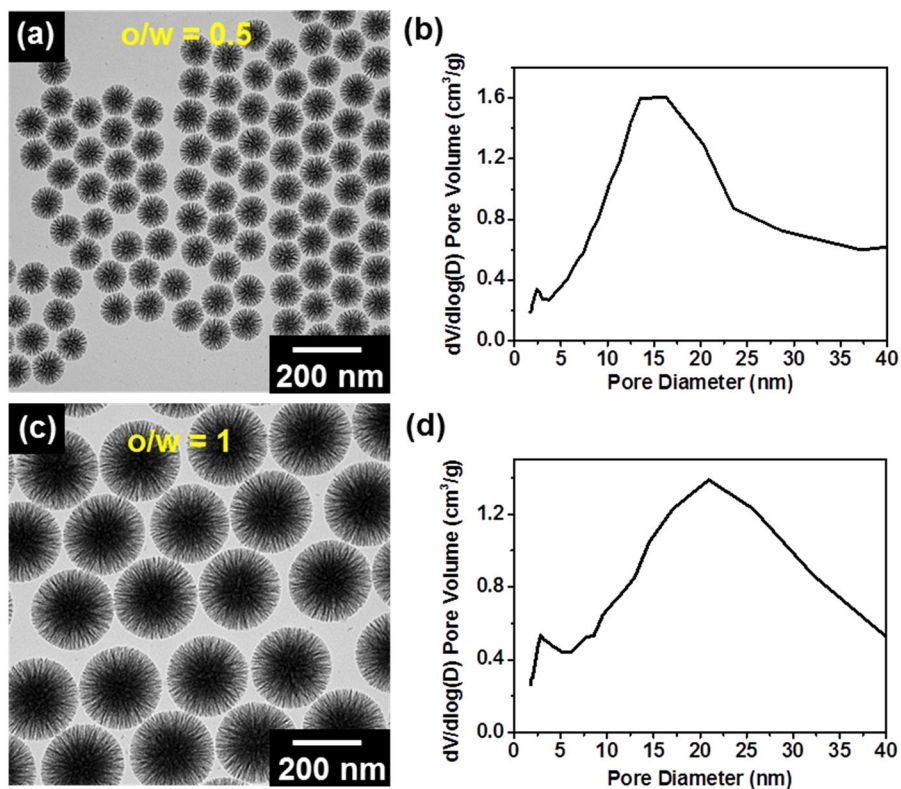


Figure 16. Effect of oil-to-water ratio; TEM images and the corresponding pore volume distribution plots of the WSNs fabricated with different oil-to-water ratio, (a, b) = 0.5, and (c, d) = 1

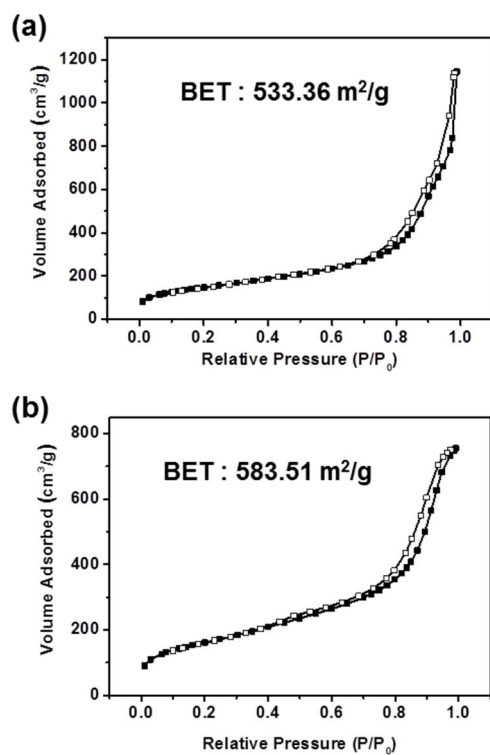


Figure 17. N_2 adsorption-desorption isotherms of the WSNs fabricated with different oil to water ratio, (a) = 0.5, and (b) = 1 in the reaction mixture (corresponding with **Figure. 4**).

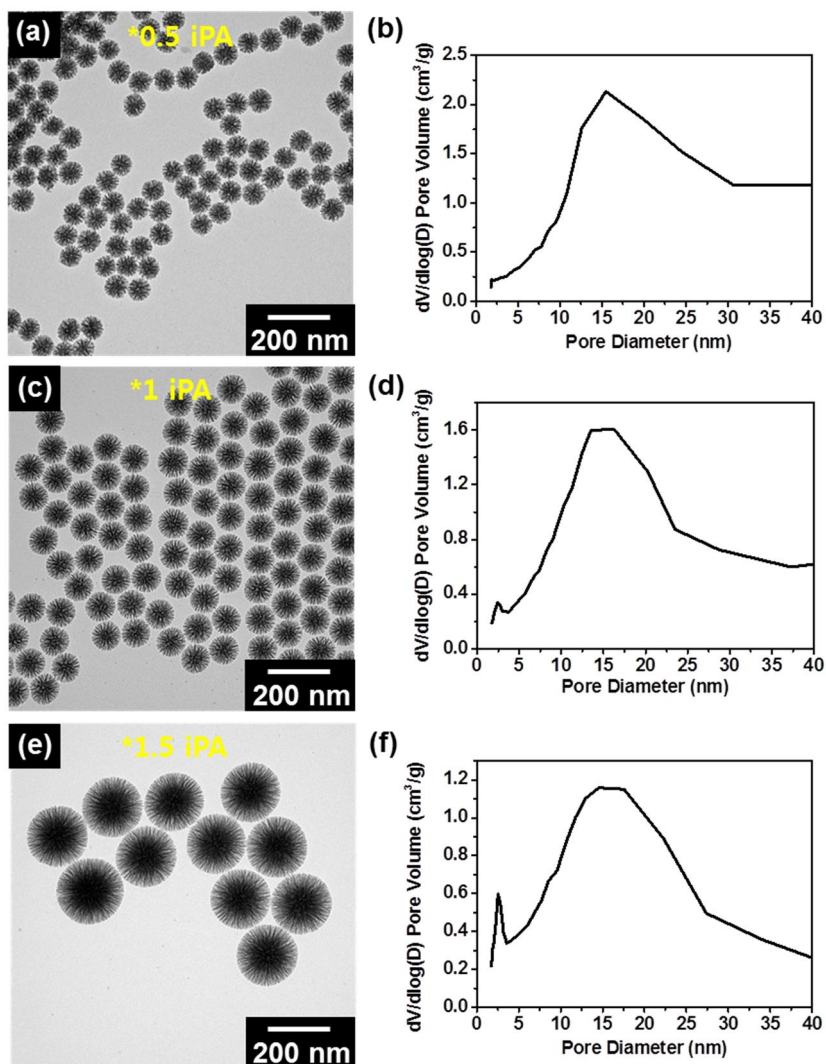


Figure 18. Effect of amount of added iso-propanol (iPA); TEM images and the corresponding pore volume distribution plots of the WSNs fabricated with different amounts of iPA, (a, b) 0.92 mL, (c, d) 1.84 mL, and (e, f) 2.76 mL iPA.

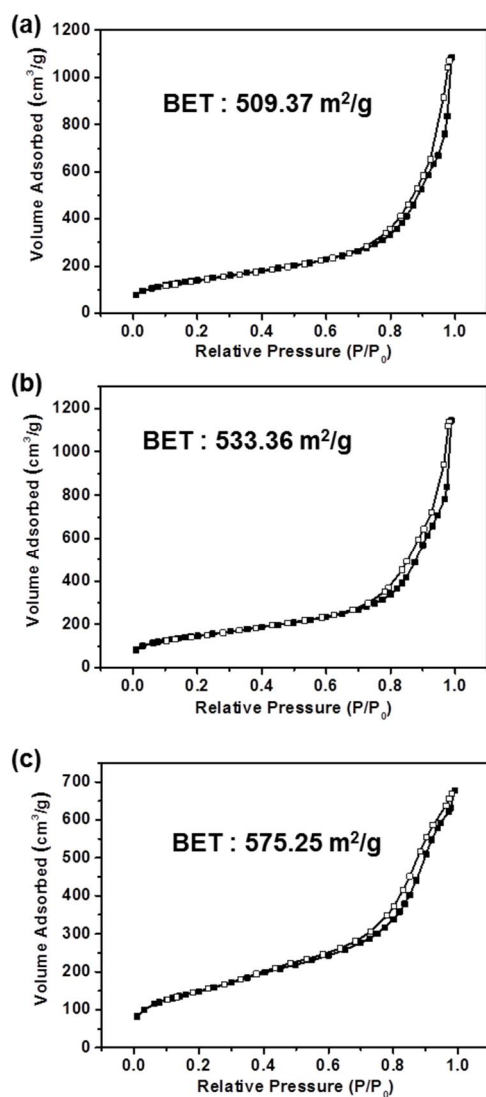


Figure 19. N₂ adsorption-desorption isotherms of the WSNs fabricated with different amounts of iPA, (a) 0.92 mL, (b) 1.84 mL, and (c) 2.76 mL iPA (corresponding with **Figure. 5**).

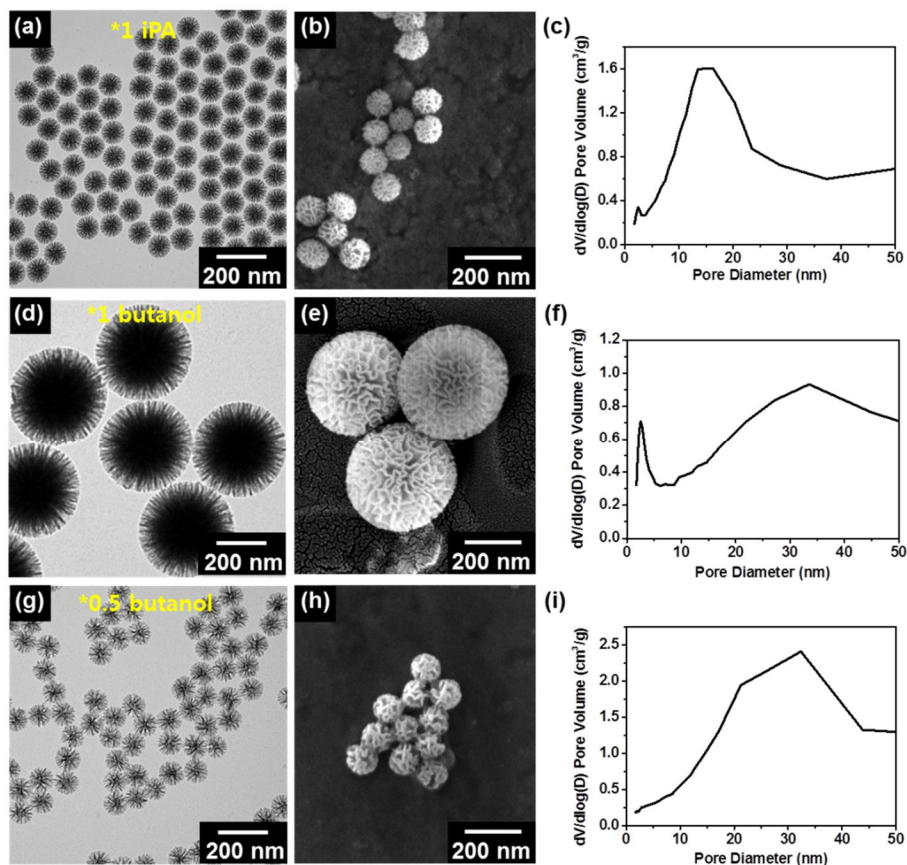


Figure 20. Effect of cosolvent; TEM images, SEM images, and the corresponding pore volume distribution plots of the WSNs fabricated with different cosolvent, (a, b, c) 1.84 ml iPA, (d, e, f) 2.2 ml butanol, and (g, h, i) 1.1 ml butanol.

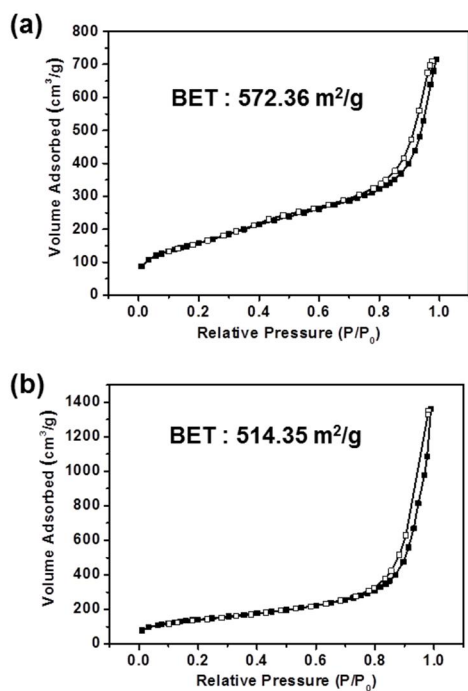


Figure 21. N₂ adsorption-desorption isotherms of the WSNs fabricated with (a) 2.2 ml and (b) 1.1 ml butanol (corresponding with **Figure 6**).

Table 1. Summary of the characteristics of the WSNs according to all experimental conditions in the manuscript.

Experimental condition			Characteristics		
O/W	Co-solvent type, addition amount [mol]	Post-reaction temperature [°C]	Diameter [nm]	Inter- wrinkle distance [nm]	BET area [m ² g ⁻¹]
0.5	0.024 mol iPA	70	100	15	533.36
0.5	0.024 mol iPA	75	210	15	583.09
0.5	0.024 mol iPA	80	330	15	616.85
0.5	0.024 mol iPA	70	100	15	533.36
1	0.024 mol iPA	70	250	21	583.51
0.5	0.012 mol iPA	70	70	15	509.37
0.5	0.024 mol iPA	70	100	15	533.36
0.5	0.036 mol iPA	70	200	15	575.25
0.5	0.012 mol Butanol	70	100	33	514.35
0.5	0.024 mol Butanol	70	400	33	572.36

All samples underwent pre-reaction for 1h at 70 °C and cooling process for 2 h at 10 °C

3.1.3. The chemical mechanical polishing performance evaluation of the WSNs as slurry abrasives

The uniformity of CMP slurry abrasive materials is an important factor for achieving high CMP performance.[86] The modified method for WSN fabrication exhibited high uniformity and high yield, and these characteristics are suitable for slurry abrasives in CMP; hence, the fabricated WSNs were tested as slurry abrasive materials. The flow rate was 100 mL min^{-1} and a $1.05\text{-}\mu\text{m}$ -thick SiO_2 layer was polished for 1 min (**Figure 22**); 100 nm monodispersed-non porous SiO_2 spheres and 100 nm monodispersed WSNs were tested, which was suitable size for slurry materials.[87, 88] For comparison, a fumed silica-based commercial oxide slurry (STAR4000, Cheil Industry Co.) was also evaluated as slurry material under the same conditions. **Figure 23** presents cross-sectional SEM and atomic force microscopy (AFM) images of the substrates after CMP with corresponding TEM images of the abrasive material used. The CMP performance evaluation was summarized in **Table 2**. The WSNs exhibited the fastest material removal rate (MRR) among the three materials. Compared with the non-porous silica nanospheres ($= 41.79 \text{ m}^2 \text{ g}^{-1}$, **Figure 24**), the significantly increased surface area of the

WSNs ($= 533.36 \text{ m}^2 \text{ g}^{-1}$) improved the contact region and, as a result, the chemical reactivity with the substrate.[46] This caused the WSNs to exhibit a faster removal rate than the spheres. Fumed silica generally exhibits poorer substrate surface roughness due to its large agglomerate and irregular shape compared with colloidal silica, but displays a faster removal rate.[89-91] However, the WSNs of colloidal silica provided a 34.2% enhanced removal rate compared with the commercial product consisting of fumed silica under same conditions. In contrast, the surface of the substrate after the CMP process was roughened in the order WSNs, spheres, and STAR4000. The WSNs and spherical colloidal silica provided a better substrate surface after CMP due to their uniformity, softness, and spherical structure, compared with the commercial product.[89] In addition, the surface roughness of the substrate after the CMP process with the WSNs was lower than that with SiO_2 spheres. The surface roughness after CMP is affected by the indentation depth of the abrasive particles.[92] The indentation depth depends on mechanical properties such as the hardness (H) and Young's modulus (E) of the absorber particles;[93] porous particles have smaller H and E than nonporous solid particles.[94] The porous WSNs were elastically deformed compared

with non-porous SiO₂ spheres during the CMP process, resulting in improved contact area with the substrate and a reduced indentation depth. Therefore, the WSNs made a better-quality substrate surface after CMP than the SiO₂ spheres. Furthermore, the WSNs were confirmed not to be structurally collapsed after the CMP process as exhibited in **Figure 25**, indicating that WSNs have stable mechanical properties under the pressures applied during the CMP process.

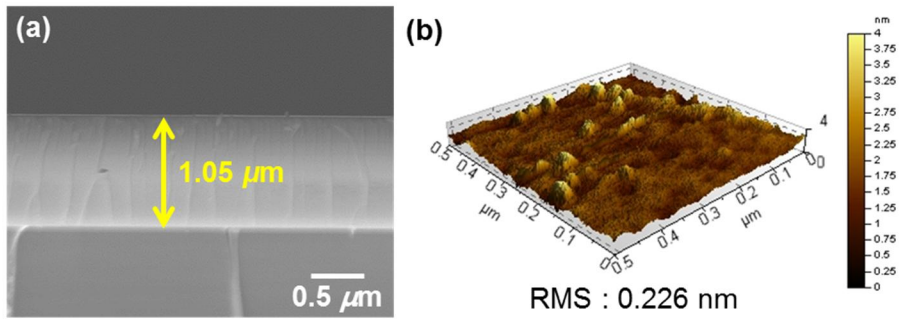


Figure 22. (a) Cross-sectional SEM and (b) 3D AFM images of the substrates before CMP process.

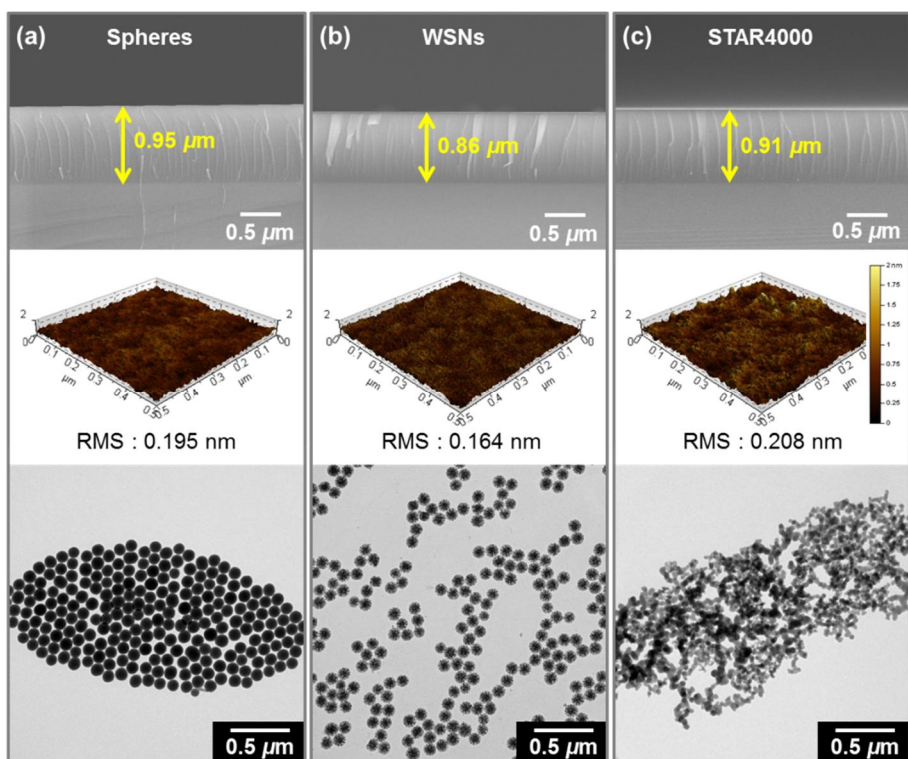


Figure 23. Cross-sectional SEM images and 3D AFM images of the substrates after CMP with corresponding TEM images of (a) monodisperse-SiO₂ spheres (100 nm), (b) monodisperse-WSNs (100 nm), and (c) STAR4000 as slurry abrasive materials.

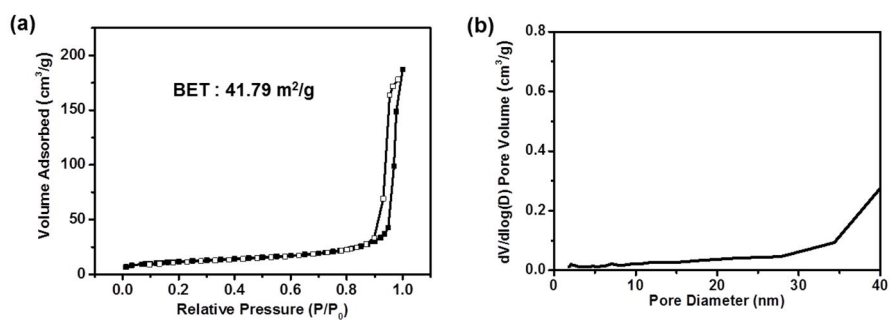


Figure 24. (a) N_2 adsorption-desorption isotherms and (b) pore volume distribution plots of 100 nm silica spheres.

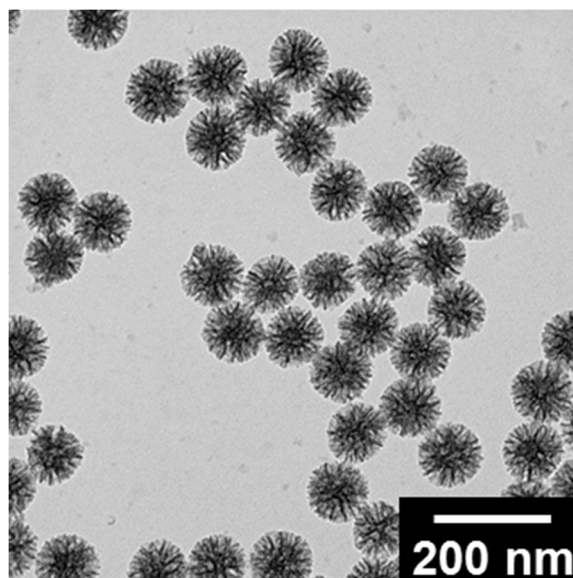


Figure 25. TEM image of WSNs after CMP process.

Table 2. Summary of MRR and surface roughness of the substrates before and after CMP.

Abrasive materials	<i>MRR</i> [Å · sec⁻¹]	<i>Surface roughness</i> [nm]
Before CMP	-	0.226
Uniform SiO ₂ spheres	16.8	0.195
Uniform WSNs	31.8	0.164
STAR4000 ^a	23.7	0.208

^a 1 wt%, pH 11 fumed silica-based commercial oxide slurry(Cheil Industry Co.)

3.1.4. Performance of dye sensitized solar cells with scattering layer of WSNs

Figure 26 describes the schematic illustration of the assembled DSSCs introduced WSNs scattering layer on the TiO₂ film of working electrode. In addition, pristine TiO₂ NPs and non-porous SiO₂ NPs were also applied to mesoporous film of working electrode, respectively, to investigate the light scattering ability of the WSNs on the performance of DSSCs. Overall thickness of the mesoporous film were controlled to around 10 – 11 μm . Cross-section SEM image of the device structure is shown in the **Figure 26b**, displaying that the thickness of TiO₂ NPs underlayer and overlayer as a scattering layer are about 7 μm and about 3.5 μm , respectively. **Figure 27** demonstrated that the mixed structure with WSNs and TiO₂ as scattering layer represented that WSNs were dispersed uniformly without any brokenness. Hierarchical mesoporous silica nanoparticles with a radial wrinkle structure (WSNs) were fabricated in the bicontinuous micro-emulsion phase in the Winsor III system.[39] The Winsor III system could be formed at a specific mixture ratio of cyclohexane and aqueous solution containing urea, CPB, and alcohol. **Figure 28** displayed

transmission electron microscopy (TEM) images of *ca.* 220 nm-diameter-silica sphere, *ca.* 220, 320, and 430 nm-diameter-WSNs (referred to herein as 220 Spheres, 220 WSNs, 320 WSNs, and 430 WSNs, respectively). The spheres were fabricated for comparison with WSNs of the same size. Brunauer, Emmett, Teller (BET) surface areas of WSNs with different sizes measured by N₂ adsorption-desorption isotherms were summarized in **Table 3**. 220 WSNs have a remarkable specific surface area (572.09 m²·g⁻¹), exhibiting significant enhanced surface area compared with SiO₂ spheres of the same size (17.26 m²·g⁻¹). The surface area of the WSNs displays a tendency to increase with increasing particle size, however, there has not been shown significant difference in values. The isotherms of WSNs exhibited H3 type hysteresis loop, and inter-wrinkle distances corresponding to pore size of WSNs were confirmed about 15 nm by BJH adsorption pore distribution plots (**Figure 29**). These results can be explained as WSNs form slip shapes and exhibit mesoporous feature.[95] These hierarchically-structured materials could be expected to provide superb light scattering ability. **Figure 30** presented diffused reflectance spectra

(DRS) investigation for confirming light scattering ability of the prepared 220 spheres, 220 WSNs, 320 WSNs, 430 WSNs. 220 WSNs revealed improved reflectance intensity over the entire region of 400-900 nm compared with sphere-shaped SiO₂ nanoparticles of the same size. Clearly, it demonstrates that light scattering is significantly enhanced by hierarchical structure, as expected. **Figure 30b** illustrates the comparison of the light scattering path in the silica sphere and the WSN. Comparing with sphere shape, multiple scattering events occur in numerous SiO₂ / air (electrolyte) interface of WSNs by hierarchical structure, leading to increase the light path length between particles.[96, 97] Moreover, the reflectance at overall visible-light region gets higher with increasing the size of nanoparticles. This tendency results from the size dependency of the light scattering effect.[98, 99] Interestingly, there was an observation that 220 nm-diameter nanoparticles (both 220 spheres and 220 WSNs), 320 WSNs, and 430 WSNs showed the characteristic photonic reflectance peaks at about 450 nm, 700 nm, and 850 nm, respectively.[100, 101] These peaks almost correspond with Mie's scattering theory that the size of spherical scattering material for an effective light

scattering is approximately half of the wavelength of incident light.[59] The photovoltaic performances of assembled DSSCs with an anode film that incorporates 220 spheres, 220 WSNs, 320 WSNs, and 430 WSNs are presented in **Figure 31**, and their photovoltaic properties are summarized in **Table 4**. There has been observed a remarkable difference on the short-circuit current (J_{sc}), but V_{oc} and FF values of all samples are similar, respectively. Compared with reference cells ($12.51 \text{ mA}\cdot\text{cm}^{-2}$), the J_{sc} values for 220 spheres ($13.71 \text{ mA}\cdot\text{cm}^{-2}$) and 220 WSNs ($14.89 \text{ mA}\cdot\text{cm}^{-2}$) were 9.59 % and 19.02 % enhancement, respectively, which is resulted from light scattering effect by incorporating large size of silica nanoparticles. The extent of J_{sc} improvement of 220 WSNs was much higher than that of 220 spheres in comparison with reference device. As discussed above in **Figure 30b**, multiple light scattering by hierarchical structure increased the light path length, and induced optical confinement. DSSCs performance in relation to the size of the WSNs was also investigated. The J_{sc} value for WSNs incorporated cells increased with increasing their sizes, thus, leading to enhance power conversion efficiency (PCE). The 430 WSNs showed the best

photovoltaic performance under our experimental condition, which are 9.53% PCE value and 30.19 % PCE enhancement in comparison to reference cells. This J_{sc} variation can be also seen in the IPCE spectra of **Figure 31b**. Compared with reference cells, DSSCs-introduced 220 spheres exhibited an improvement in quantum efficiency (QE), particularly in the long wavelength region (> 600 nm) owing to the light scattering effect. The 220 WSNs showed higher QE over the entire wavelength range than 220 spheres of the same size. While the enhancement of QE at short wavelength (< 400 nm) was ascribed to large adsorption of dye, QE improvement at long wavelength (> 600 nm) was attributable to the enhancement of light scattering effect.[102] It could be checked through IPCE enhancement factors based on the 220 spheres (**Figure 31c**). A sharp increase was noted in the long wavelength region (> 550 nm).[103] This was similar to the DRS enhancement factor based on 220 spheres that increases with increasing wavelength (**Figure 31d**). The N719 dye exhibited low absorbance in the long wavelength range, indicating that the amount of dye adsorption is not an important factor in this wavelength region.[102] Therefore, it could be

explained that effect of light scattering is dominant in the IPCE of the long wavelength region. In addition, the QE value in IPCE spectra presented a tendency to increase with particle size, especially in the long wavelength region. Thus, light scattering depends on the size of the WSN, given similar BET areas. On the other hand, 220 spheres showed QE value similar to that of the reference cells in the short wavelength region, although the amount of dye adsorption of 220 spheres was lower than that of reference cells due to lower surface area (**Table S2**). This could be explained the scattering effect, which was not observed in reference cells, could compensate for the loss from the low surface area of the 220 spheres. Therefore, light scattering effect can influence IPCE value over the entire region, but dye adsorption is the critical factor in the short wavelength region regardless of the light scattering intensity when a certain extent of light scattering is given.

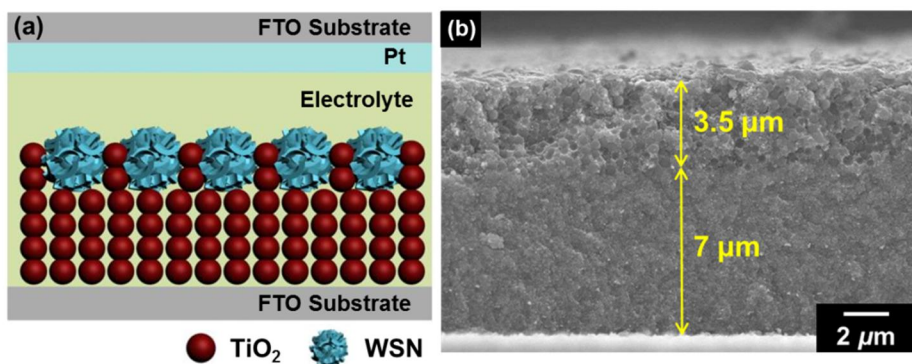


Figure 26. (a) Schematic illustration and (b) cross-section SEM image of the device structure of DSSCs containing TiO_2 NPs under-layers and WSNs over-layer as a scattering layer.

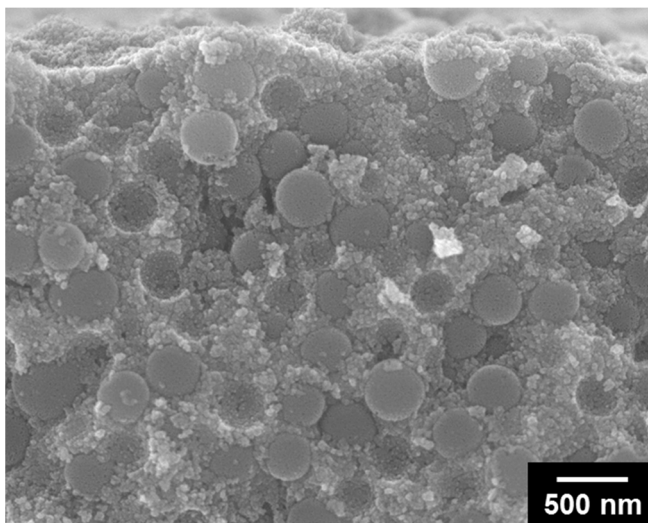


Figure 27. SEM image of WSNs over-layer as a scattering layer of working electrode in the DSSCs device.

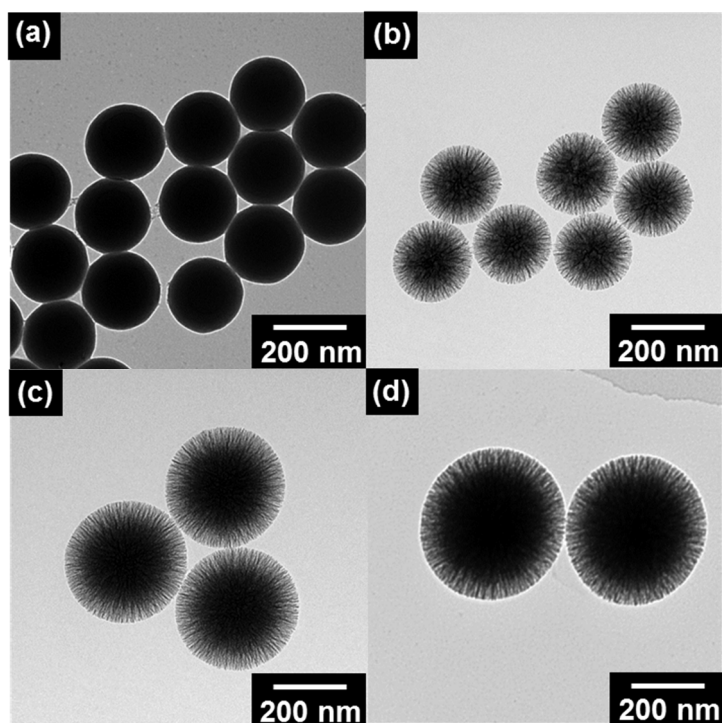


Figure 28. TEM images of (a) 220 nm silica spheres, (b) 220 nm WSNs, (c) 320 nm WSNs, and (d) 430 nm WSNs.

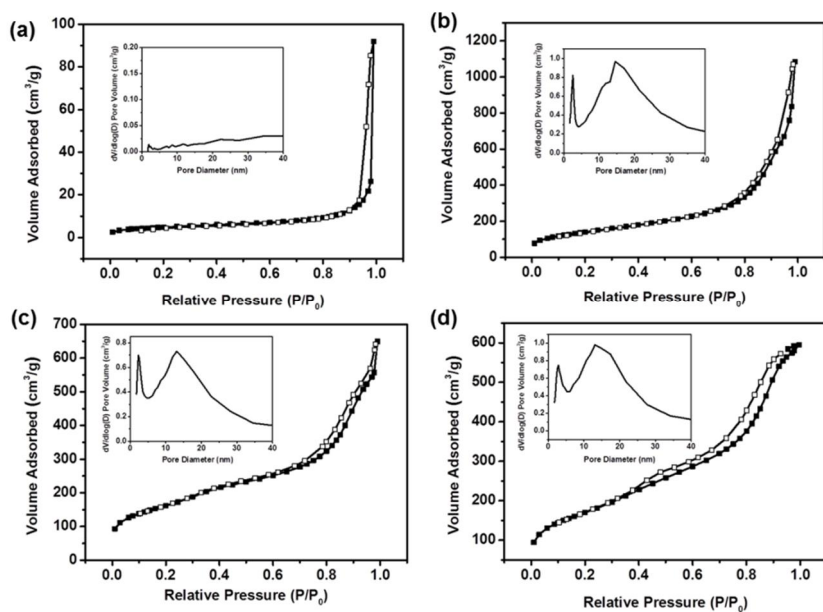


Figure 29. N_2 adsorption-desorption isotherms and pore volume distribution plots (inset) of (a) 220 nm silica spheres and WSNs with (b) 220 nm, (c) 320 nm, (d) 430 nm diameters.

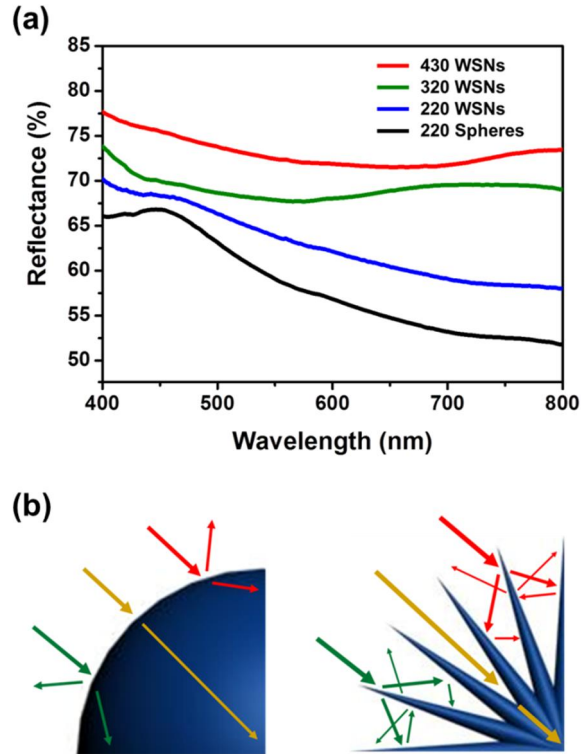


Figure 30. (a) Diffuse reflectance spectra for 200 nm silica spheres and WSNs with various sizes (220, 320, 430 nm). (b) Schematic illustration of the light scattering effect within spheres and WSNs

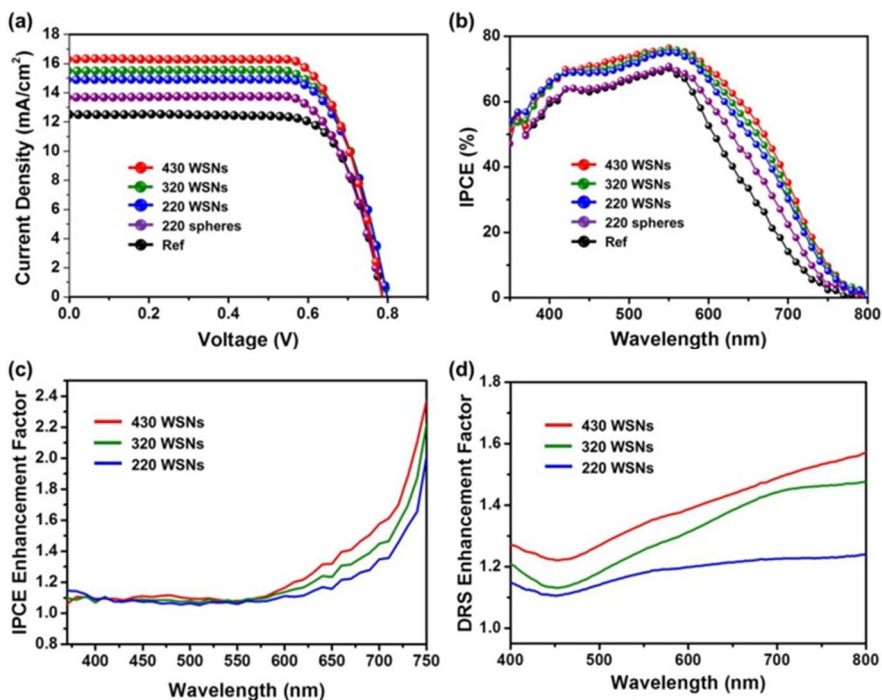


Figure 31. (a) Current density-voltage (J–V) characteristics and (b) Incident photon-to-current efficiency (IPCE) spectra for DSSCs based on WSNs with various sizes and 220 nm silica spheres; (c) IPCE enhancement factor ($=\text{IPCE}_{\text{sample}}/\text{IPCE}_{220\text{spheres}}$) based on the 220 spheres, and (d) DRS enhancement factor ($=\text{DRS}_{\text{sample}}/\text{DRS}_{220\text{spheres}}$) based on the 220 spheres.

Table 3. Summary of BET analysis of the silica spheres and WSNs with various sizes

Sample	BET [m² g⁻¹]	Inter-wrinkle distance^a [nm]
220 Spheres	17.26	—
220 WSNs	572.09	10-20
320 WSNs	585.25	10-20
430 WSNs	592.85	10-20

^a Corresponding to a wide peak in BJH pore distribution plots; there are two peaks in the BJH plot, consisting of a sharp peak (2 nm) and a wide band (ca. 15 nm)

Table 4. Summary of Photovoltaic properties of WSNs and silica spheres-based DSSCs

Sample^a	J_{sc} [mA/cm²]	V_{oc} [V]	FF	η^b [%]
Ref ^c	12.51	0.79	0.74	7.32
220 Spheres	13.71	0.79	0.74	7.92
220 WSNs	14.89	0.80	0.75	9.01
320 WSNs	15.50	0.80	0.75	9.32
430 WSNs	16.31	0.79	0.74	9.53

^aActive area of the assembled DSSC samples is 0.16 cm²; ^bPower conversion efficiency; ^cDSSC sample assembled without scattering layer.

Table 5. Summary of the dye adsorption amount on scattering layer of WSNs and silica spheres-based DSSCs

Sample	Dye adsorption amount [$\times 10^{-7}$ mol \cdot cm $^{-2}$]
Ref	1.000
220 spheres	0.891
220 WSNs	0.966
320 WSNs	0.972
430 WSNs	0.988

3.2. Fabrication of Hierarchical Mesoporous Wrinkled Silica Nanoparticle based-SiO₂/TiO₂ Hollow Nanoparticles

3.2.1. Fabrication of hierarchical mesoporous wrinkled silica nanoparticle based-SiO₂/TiO₂ hollow nanoparticles

Figure 32 describes the overall experimental synthetic process for the fabrication of the WSN based-SiO₂/TiO₂ hollow nanoparticles (hereafter referred to as ‘W-HNP’). First, uniform WSNs of 100 nm size serving as a core hard template for the final material W-HNP were fabricated based on the Winsor III system.[78] Then, the mesoporous TiO₂ shell was coated on the WSN to fabricate WSN based-SiO₂/TiO₂ core/shell nanoparticle (hereafter referred to as ‘W-STCS’) by the sol-gel method using TTIP as precursor.[98] WSN as core template of the W-STCS was etched by sonication using NH₄OH solution to obtain W-HNPs.[104] At the beginning of the etching process, silica core was dissolved due to ammonium hydroxide by weakening siloxane bonds and coordinating hydroxide ion with Si atoms.[105] Contrary to SiO₂, TiO₂ did not dissolve due to its chemical inertness under the condition.[106] The dissolved SiO₂ by ammonia was re-deposited on the TiO₂ shell by Ostwald ripening, resulting in the formation of the

SiO₂/TiO₂ shell.[107] Finally, the fabrication of W-HNP was completed.

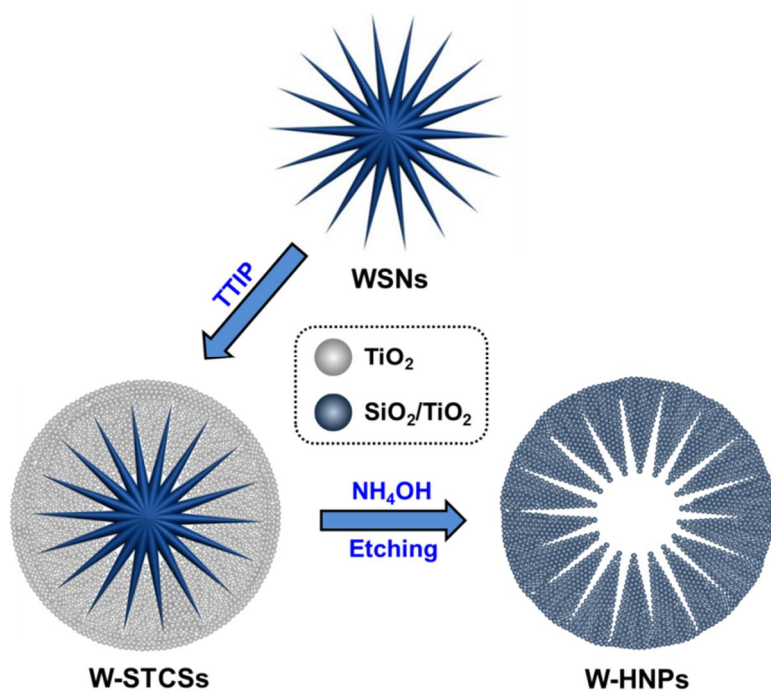


Figure 32. Schematic illustration of the formation mechanism of the WSN-SiO₂/TiO₂ hollow nanoparticles.

3.2.2. Characterization of hierarchical mesoporous wrinkled silica nanoparticle based-SiO₂/TiO₂ hollow nanoparticles

Figure 33 represented microscopy images of each material corresponding to the synthetic process as shown in **Figure 32**. WSNs with uniform diameters of 100 nm were displayed in the **Figure 33a**. The reason for preparing 100 nm sized- WSN was that the size of the WSN should be at least 100 nm for hierarchical structure, derived from the WSNs, to be recognized from the inner surface of the shell of W-HNP. 80 nm sized- WSNs were attempted to fabricate W-HNPs, but the hierarchical structure of inner surface of the W-HNP shell was not observed clearly as reflected in **Figure 34**. The TEM image of the W-STCS represented that the TiO₂ shell was uniformly coated on the WSN. The particle size of W-STCS was 120 nm, which indicated that the thickness of the TiO₂ shell was about 10 nm. **Figure 33c** exhibited TEM image of the W-HNPs, and it was confirmed that the WSNs were successfully etched while maintaining the inner surface of the shell of the W-HNP in a hierarchical structure, which was derived from the WSN. The particle size of W-HNP was *ca.* 140 nm and thus, the thickness of the shell was *ca.* 20 nm. This indicated that the thickness of the shell increased after etching process. It was due to the

sonication mediated etching and re-deposition method for W-HNP fabrication.[104] Since the silica experienced condensation and re-deposition on the TiO_2 shell surface during the etching process, the shell thickness slightly increased compared to that of W-STCS. **Figure 33d** manifested the SEM image of the W-HNP, and the shell of the HNP formed with aggregates of small $\text{SiO}_2/\text{TiO}_2$ particles by the sol-gel method.[108]

In addition, the W-HNP fabricated according to the amount of TTIP added was investigated in **Figure 35**. ‘*1 TTIP’ denotes the addition amount of TTIP corresponding to 4.32 times of WSN mass. The addition of TTIP was adjusted to *0.5, *0.75, *1, and *2 TTIP. In the case of *0.5 TTIP, the WSN as the core portion was not etched, and particles which lost the original shape of WSN were observed. Due to the too low amount of TTIP added, a sufficient amount of TiO_2 shell was not formed on the WSN surface to allow silica to be re-deposited during the etching process. Therefore, silica could not diffuse into the TiO_2 shell after condensation. In the case of *0.75 TTIP, W-HNP with a shell thickness of < 10 nm was formed, and the wrinkled inner surface of the shell derived from WSNs was well observed. However, thin TiO_2 shells tend to break easily during the

etching process without maintaining their shape. Case of *2 TTIP showed that the WSNs were not completely etched. It was attributable that the thick TiO_2 shell formed by the addition of large amounts of TTIP prevented NH_4OH for silica etching from effectively diffusing into the shell.

Scanning transmission electron microscopy-energy dispersive spectroscopy (STEM-EDS) was conducted to investigate the elemental distribution in the W-HNP. **Figure 36** displayed STEM image of the W-HNP, showing a 100 nm hierarchical pore and a 20 nm thick shell. Dot distributions of Si, Ti, and O elements were represented in **Figure 36b-d**, respectively. The dots of the three elements revealed the entire distribution of the particles, but they were particularly dense in the shell. Furthermore, the distribution of the elemental dots of the W-HNP could be confirmed clearly by comparing the STEM-EDS images of the WSN and W-STCS shown in **Figure 37** and **Figure 38**, respectively. Therefore, it could be seen that the W-HNP was a hollow structured-particle and the shell was composed of SiO_2 and TiO_2 through STEM-EDS analysis of W-HNP.

To further characterize of WSNs and WSN-derivatives, Brunauer–Emmett–Teller (BET) and Barrett–Joyner–Halenda (BJH)

analyses of WSNs, W-STCSs, and W-HNPs were performed as shown in **Figure 39** and summarized in **Table 6**. WSNs had high surface and pore volume, which were $533.36 \text{ m}^2\cdot\text{g}^{-1}$ and $1.77 \text{ cm}^3\cdot\text{g}^{-1}$, respectively. However, the surface area ($= 463.36 \text{ m}^2\cdot\text{g}^{-1}$) and the pore volume ($= 0.44 \text{ cm}^3\cdot\text{g}^{-1}$) decreased after the TiO_2 was coated on the WSNs. Although the TiO_2 shell reflected mesoporous structure composed of 2.5 nm sized pores, both surface area and pore volume of W-STCS were reduced because the pores of WSNs with relatively higher surface area were filled by TiO_2 . In the case of W-HNP, surface area and pore volume were improved by the etching of WSNs compared to W-STCS. Various pore sizes were observed in the BJH plot of the W-HNP; pore size of 2.5 nm corresponded to pore of the TiO_2 shell.[109] Pore sizes of 5 nm, 7.5 nm, and 10 nm should be originated from the hierarchical structure of the inner surface of the shell of W-HNPs. The pore size of 80 - 100 nm corresponded to the diameter of the inner pore of the W-HNP.

In order to verify the ER performance according to the morphology, 100 nm sized non-porous SiO_2 spheres (hereafter referred to as 'Spheres') of the same size as WSNs were prepared *via* Stöber method and sphere based- $\text{SiO}_2/\text{TiO}_2$ core/shell nanoparticles

(hereafter referred to as 'S-STCSs') and sphere based-SiO₂/TiO₂ hollow nanoparticles (hereafter referred to as 'S-HNPs') were also fabricated using SiO₂ spheres as presented in **Figure 40**. In addition, the amount of TTIP was adjusted to equal the shell thickness of W-HNP. BET analysis of SiO₂ spheres and their derivatives were revealed in **Figure 41**. Interestingly, spheres represented the different tendency to the case of the foregoing WSNs. Owing to the non-porous structure of the SiO₂ spheres, it was confirmed that the surface area and pore volume were improved after the TiO₂ shell was coated on the SiO₂ spheres. Unlike W-HNPs, S-HNPs were confirmed to have only a pore size of 2.5 nm corresponding to the pores of TiO₂ shell and a pore size of 100 nm corresponding to the size SiO₂ spheres.

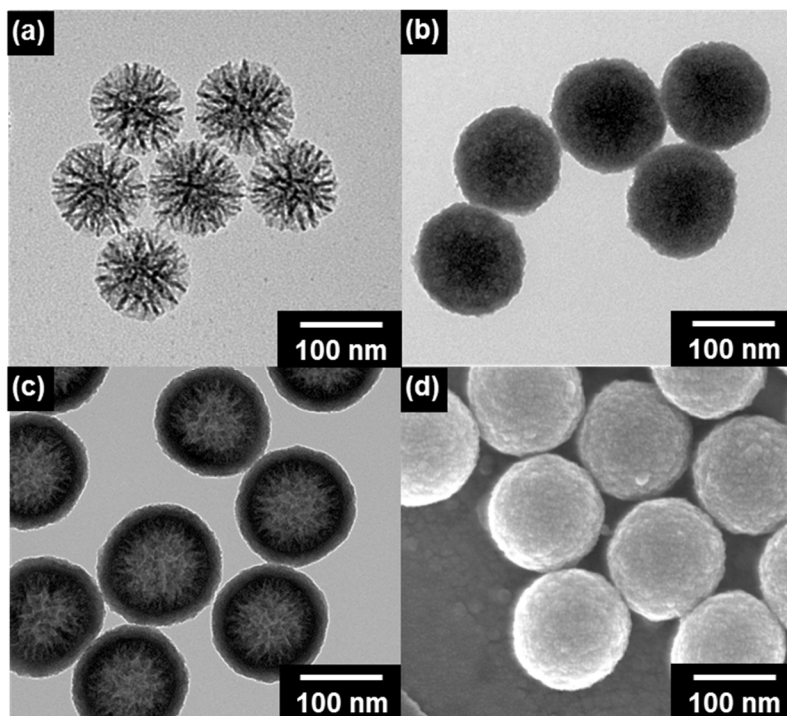


Figure 33. Transmission electron microscopy (TEM) images of (a) WSN, (b) W-STCS, and (c) W-HNP. (d) Scanning electron microscopy (SEM) image of W-HNP.

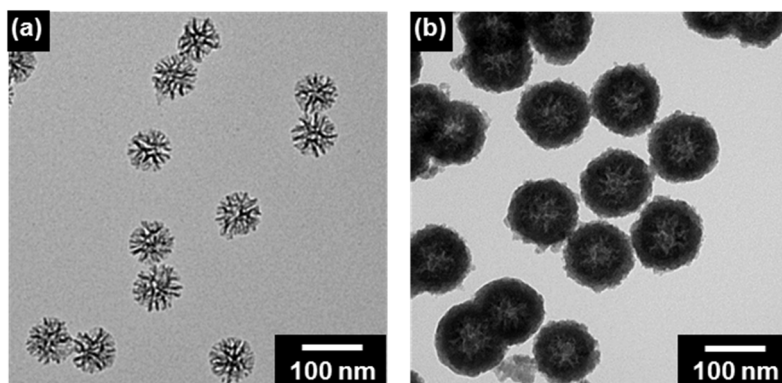


Figure 34. TEM images of (a) the 80nm-diameter-WSNs and (b) W-HNPs fabricated with the 80nm-diameter-WSNs.

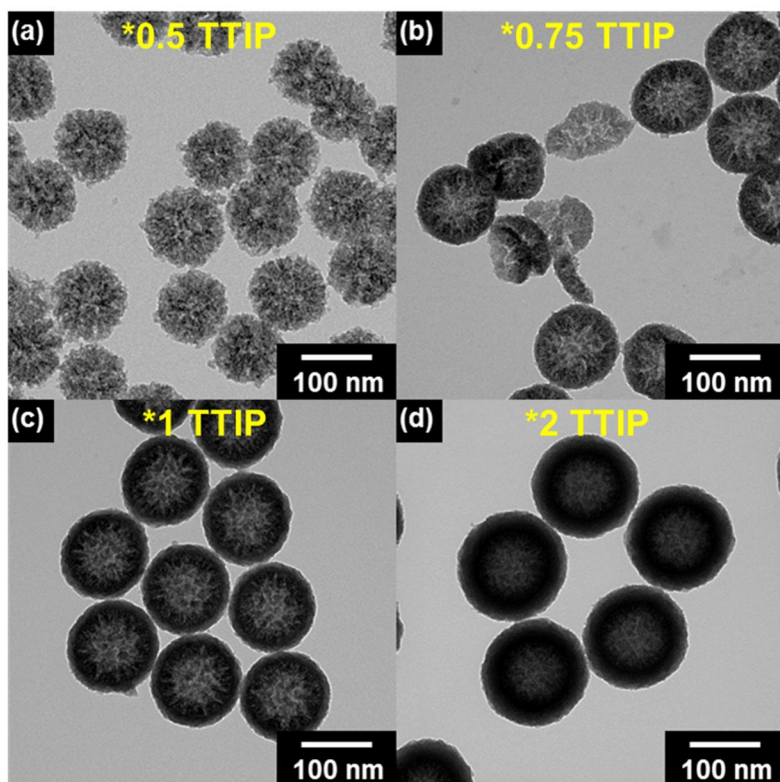


Figure 35. TEM images of the W-HNPs fabricated with different amount of TTIP.

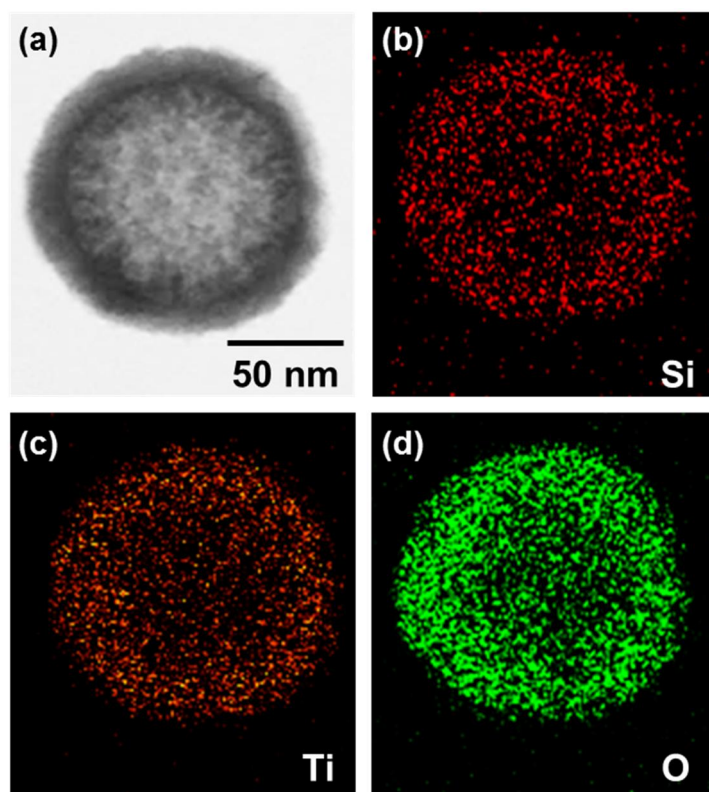


Figure 36. STEM-elemental-mapping images of W-HNP.

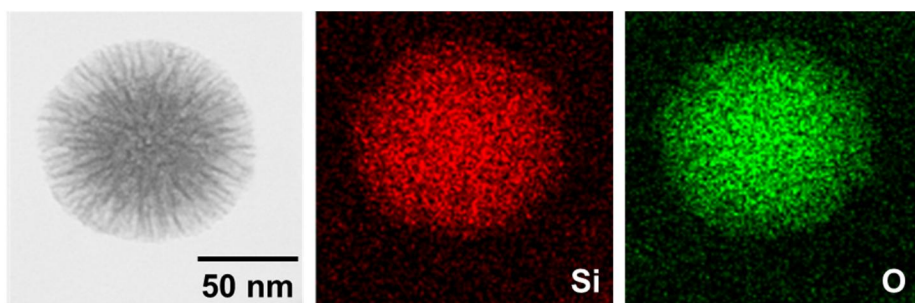


Figure 37. STEM-elemental-mapping images of WSN.

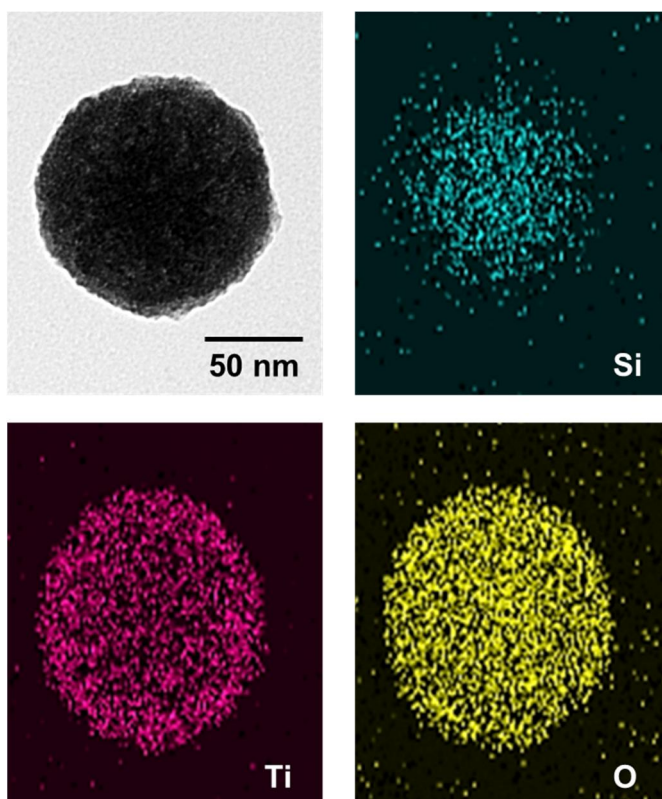


Figure 38. STEM-elemental-mapping images of W-STCS.

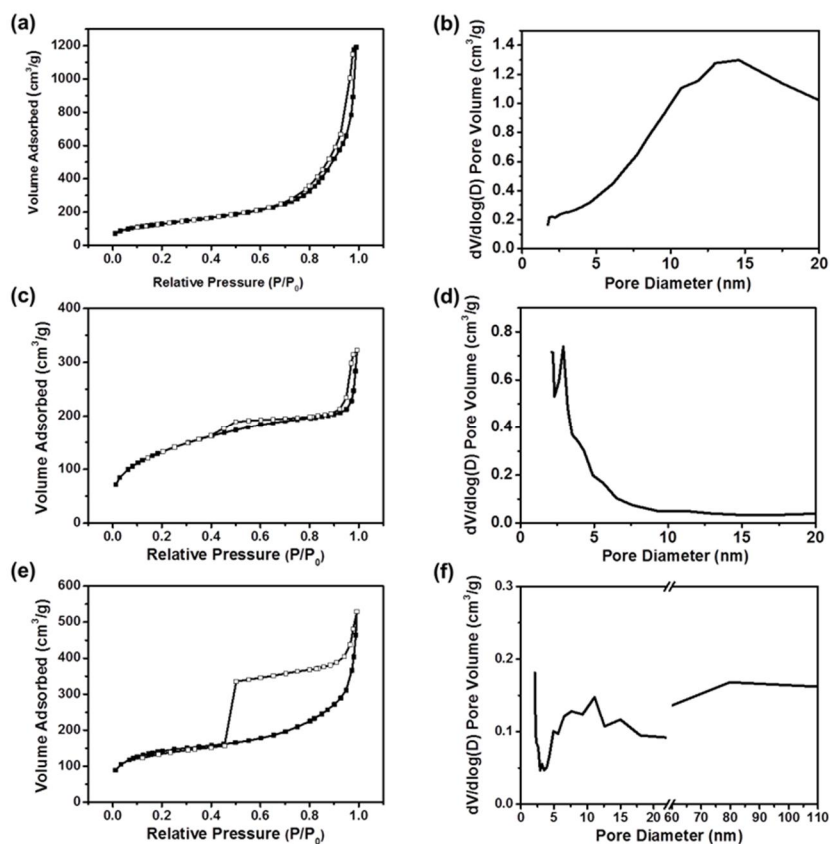


Figure 39. N_2 adsorption-desorption isotherm and pore volume distribution plots of (a, b) WSNs, (c, d) W-STCSs, and (e, f) W-HNPs.

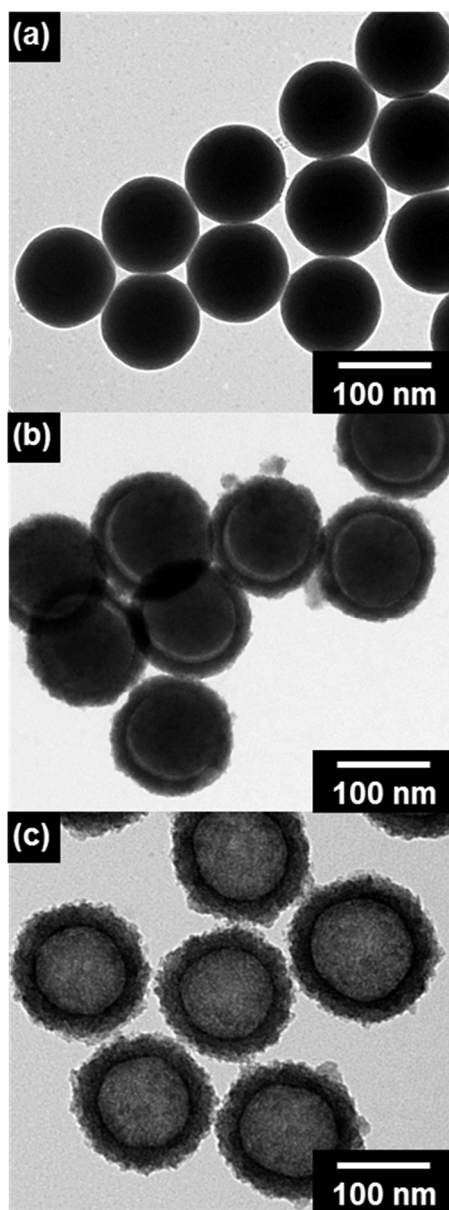


Figure 40. TEM images of (a) SiO₂ spheres, (b) S-STCS, and (c) S-HNPs.

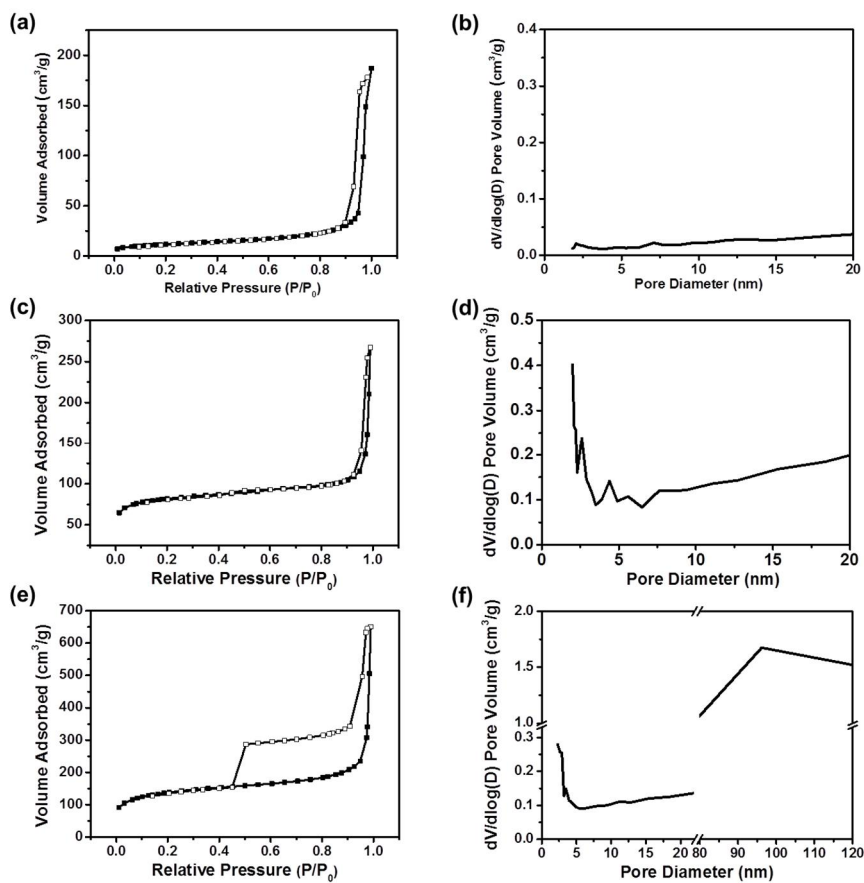


Figure 41. N_2 adsorption-desorption isotherm and pore volume distribution plots of (a, b) Spheres, (c, d) S-STCSs, and (e, f) S-HNPs.

Table 6. Summary of BET analysis of WSNs, Spheres, and their derivatives.

Samples	BET surface area [m² g⁻¹]^a	Pore volume [cm³ g⁻¹]^b
Sphere	41.79	0.29
S-STCS	271.39	0.33
S-HNP	461.96	1.03
WSN	533.36	1.77
W-STCS	463.36	0.44
W-HNP	501.29	0.84

^a Calculated by BET method; ^b Total pore volume.

3.2.3. Electrorheological properties of electrorheological fluid based on hierarchical mesoporous wrinkled silica nanoparticle based-SiO₂/TiO₂ hollow nanoparticles

According to the previous studies, two key intrinsic characteristics of materials affecting the ER performance were known as dispersion stability and dielectric properties.[109] In general, it is known that materials with increased dispersion stability may show high ER performance due to improved particle mobility in dispersing medium.[110] Dispersion stabilities of WSN, W-STCS, and W-HNP were examined by determination of sedimentation ratio (R) in silicone oil medium at concentrations of 3.0 wt% as displayed in **Figure 42**. Also, dispersion stability of sphere and its derived materials (S-STCS and S-HNP) were assessed for comparison purpose. All particles displayed abrupt sedimentation behavior until 20 h. After that, gradual subsiding of particles was observed and equilibrium state was reached at 90 h. Each material sedimented slightly differently because of their different characteristics, such as surface area, pore volume, composition, and morphology. In case of WSN and its derived materials, WSN showed the highest dispersion stability of 0.89 (meaning *ca.* 85 % of materials were stably dispersed in final state),

which was in accordance with the highest surface area and pore volume determined from the BET and BJH analysis. After the TiO_2 coating process, dispersion stability of W-STCS decreased to 0.77 due to the addition of relatively heavy TiO_2 shell and their filling of hierarchical WSN morphology, which also lessen the surface area and pore volume. However, dispersion stability of final W-HNP was re-increased to 0.83 after the etching of core SiO_2 part, inferring the formation of internal hollow structure and vacant spaces within TiO_2 shells. In this regard, it can be concluded that final W-HNP was successfully prepared as highly dispersive material even after the coating of TiO_2 material. However, sphere and its derived S-STCS and S-HNP displayed similar, but slightly different dispersion stability changing trend with the coating and etching processes compared to WSN and their series of materials. Firstly, sphere demonstrated dispersion stability of 0.79, which was lower than WSN. Such relatively low dispersion stability of sphere compared to WSN was due to the flat surface of sphere without any porosity. Continuously, dispersion stability of S-STCS was even decreased to 0.74, which was similar decreasing behavior as W-STCS. However, it was noticeable that the dispersion stability of S-HNP greatly improved to 0.85,

passing the dispersion stability of W-HNP and even the starting sphere material. The difference in the dispersion stability of final hollow W-HNP and S-HNP can be explained by the different morphology between two materials. Compared to flat internal surface of S-HNP, W-HNP of the same shell thickness as S-HNP had higher internal surface area originating from the hierarchical structure, which increased the internal loading capacity of TiO_2 materials. After the etching process, S-HNP lost large amount of core SiO_2 leaving only TiO_2 shell behind, but W-HNP is left with TiO_2 shell and hierarchical inside. Thus, dispersion stability of S-HNP was higher than W-HNP and starting sphere. Considering these results, dispersion stabilities of W-HNP and S-HNP were both improved by removing SiO_2 part, but different amounts of leftover TiO_2 caused the difference in dispersion stability of two materials. As discussed earlier, TiO_2 is known as high dielectric material, thus amount of TiO_2 affected the dielectric properties of materials.

To gain insight into the dielectric properties, dielectric constant (ϵ') and loss factor (ϵ'') of WSN, sphere, and their derived materials were examined as a function of electric field frequency as exhibited in **Figure 43**. It is known that dielectric characteristics greatly affect the

polarization abilities of materials under applied E field strength.[111, 112] In specific, achievable polarizability ($\Delta\epsilon$, polarization tendency) and relaxation time (λ , polarization rate) can be interpreted from the ϵ' and ϵ'' curves. Generally, materials with large $\Delta\epsilon$ and short λ are known to exhibit high ER performance under E field.[113, 114] The $\Delta\epsilon$ of can be determined by the differences between fictitious ($\epsilon_0, f \rightarrow 0$) and static ($\epsilon_\infty, f \rightarrow \infty$) dielectric constants to provide information on polarization tendency of material. Determined $\Delta\epsilon$ for WSN, W-STCS, and W-HNP were 1.12, 2.11, and 2.42, respectively. By introducing the high dielectric TiO_2 layer, W-STCS manifested enhanced polarizability compared with that of SiO_2 composed WSN. Further increment in $\Delta\epsilon$ was discovered in W-HNP than W-STCS due to combined effect of increased surface area for charge accumulation and lowered amount of low dielectric SiO_2 part after the etching process. In addition, λ of materials were evaluated by the following equation: [115]

$$\lambda = \frac{1}{2\pi f_{\max}}$$

, where f_{\max} is obtained from maximum frequency of the ϵ'' curves. Determined λ of WSN, W-STCS, and W-HNP were 2.0×10^{-3} , 6.0×10^{-4} , and 1.0×10^{-4} s, respectively. These results also suggested that

W-HNP had faster polarization rate than precursor materials of WSN and W-STCS attributed to increased amount of polarizable sites. By one-to-one comparison (*e. g.* WSN to sphere), WSN and its derived W-STCS and W-HNP showed larger $\Delta\epsilon$ and shorter λ than sphere, S-STCS, and S-HNP due to the increased surface area and amount of loaded TiO_2 arose from the hierarchical morphology of WSN. Detailed dielectric properties of materials were summarized in **Table 7**. Judging from these results, unique hierarchical morphology of WSN as well as each synthesis steps including TiO_2 coating and etching of SiO_2 effectively enhanced the dispersion stability and dielectric properties of final W-HNP materials to be suitable in ER applications.

The ER activities of sequentially prepared WSN, W-STCS, and W-HNP-based ER fluids were investigated by controlling various parameters including shear rate, E field strengths, and E field on-off test. For the comparison purpose ER activities of sphere, S-STCS, and S-HNP-based ER fluids were also evaluated. Shear stress curves (*i. e.* flow curves) of ER fluids were examined as a function of shear rate under an E field strength of 3.0 kV mm^{-1} in **Figure 44a**. With the applied E field strength, all ER fluids exhibited shear stresses due to the formation of fibril-like structures induced by the electrostatic force.

In the low shear rate region, shear stresses of all ER fluids displayed Bingham plastic like behavior marked by the plateau curves.[116] Such behavior was attributed to the balancing between formation and deformation of fibril-like structures by electrostatic and hydrodynamic forces.[117] After passing the critical shear rate, shear stresses showed Newtonian fluid-like behavior of proportional increment of shear stress with the increasing shear rate in which indicating the domination of hydrodynamic force over electrostatic force. It was clearly observed that ER activities of materials increased in the order of WSN, W-STCS, and W-HNP, which was in accordance with sequential preparation steps. Particularly, W-STCS showed higher ER performance than WSN due to increment in aforementioned dielectric properties by addition of high dielectric TiO_2 layer onto the outermost shell. Furthermore, W-HNP showed higher shear stress than WSN and W-STCS by the etching of core SiO_2 , which improved the dispersion stability and dielectric property. Also, similar ER activity trend was observed for sphere-, S-STCS-, and S-HNP-based ER fluids. Owing to the improved dielectric properties and dispersion stability, S-HNP displayed enhanced ER performance than sphere and S-STCS materials. Notably, WSN-derived materials exhibited further

improvement in ER activity compared to sphere-derived materials. These distinguished ER activities of two sequential sets of materials were may attribute to the differences in their morphologies. In particular, WSN was synthesized as unique hierarchical structures with high polarizable surface area to exhibit enhanced ER activity than flat-surfaced sphere material. Furthermore, W-HNP manifested higher ER performance than S-HNP due to the hierarchically structured core parts. Because of hierarchically arrayed inner surfaces, W-HNP can provide more polarizable sites than S-HNP, leading to stronger interactions between particles and stronger ER activity. Tentative polarization and particle interaction of W-HNP and S-HNP is described in **Figure 44b**.

To further investigate the ER activities, yield stress of ER fluids were measured as a function of E field strength at fixed shear rate of 0.1 s^{-1} as reflected in **Figure 44c**. All ER fluids manifested increased yield stresses with increasing E field strength. Yield stresses were proportionally increased by *ca.* 2.0 power of E field strength up to 1.0 kV mm^{-1} of E field strength. After passing 1.0 kV mm^{-1} , yield stresses were increased by *ca.* 1.5 power of E field strength. These distinguished increasing of yield stresses at intervals back and forth of

1.0 kV mm⁻¹ matched the typical behaviors of ER fluids under E field strengths. Also, stable yield stresses were measured up to 4.0 kV mm⁻¹ to verify the stability of ER fluids. The reversibility and reproducibility of ER fluids were assessed by real time on-off test as shown in **Figure 44d**. All ER fluids showed zero ER activity (less than 1.0 Pa) without E field application (off state). With applied E field (on state), ER fluids manifested immediate increase in yield stress. By cutting off the E field, all yield stresses instantly returned to the initial state. Second cycle of on-off test also displayed similar increase and decreasing behavior of yield stress to illustrate the reversibility and reproducibility of ER fluids.

The fibril-like formations in W-HNP- and S-HNP-based ER fluids were analyzed by optical microscopy (OM) at an applied E field strength of 1.0 kV mm⁻¹. Representative OM images of two materials are shown in **Figure 45**. In the absence of an E field, the W-HNPs and S-HNPs were well distributed in the silicone oil medium. When an E field was applied, both materials displayed a sudden formation of fibril-like structures, which were responsible for the ER activity. Noticeably, the fibril-like structures of the W-HNPs were stronger and more rigid than those of the S-HNPs; this was in good agreement with

the ER behaviors. These experimental results clearly illustrate the potential of W-HNPs as practical ER materials, given their unique morphology.

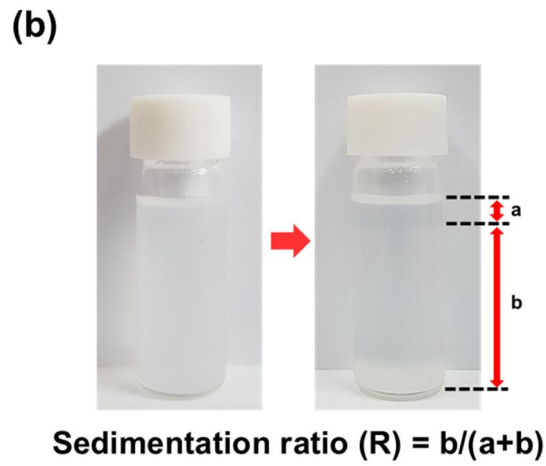
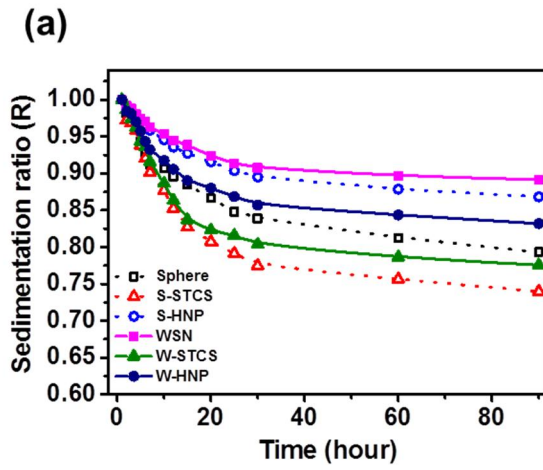


Figure 42. (a) Sedimentation ratio (R) of sphere- and WSN-derived materials-based ER fluids in silicone oil (3.0 wt%) and (b) Graphical illustration and definition of sedimentation ratio.

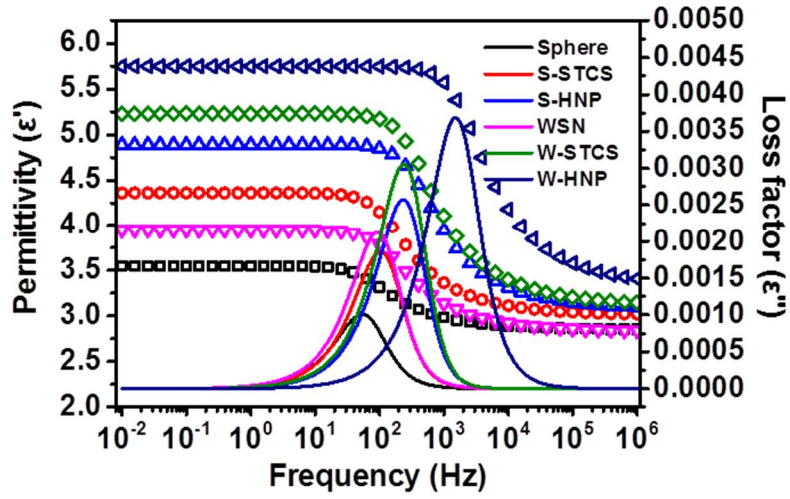


Figure 43. Dielectric constant (ϵ') and loss factor (ϵ'') of sphere- and WSN-derived material-based ER fluids as a function of electric field frequency (f).

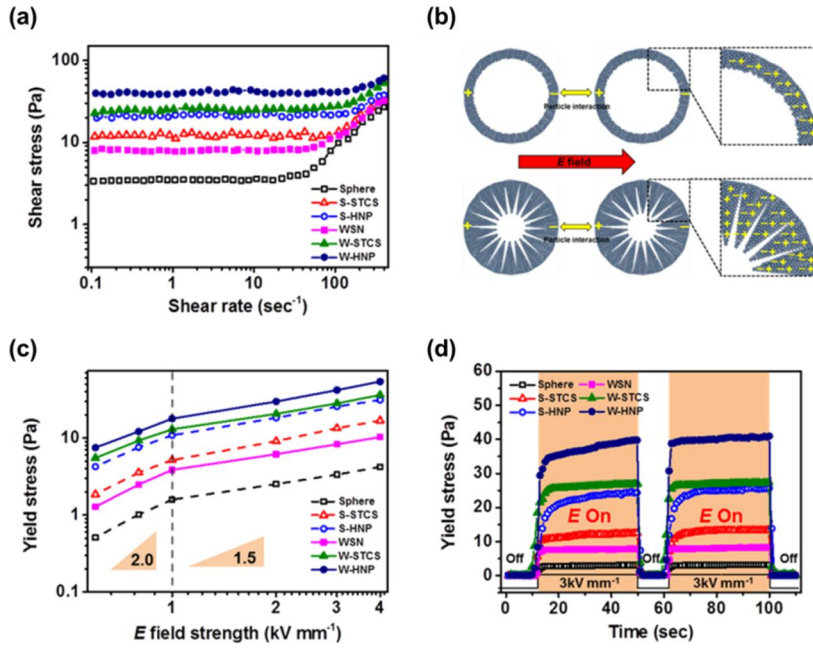


Figure 44. (a) Electrorheological activities of sphere- and WSN-derived ER fluids WSN, and TiO_2 -coated materials as a function of shear rate (3.0 wt%, 3.0 kV mm^{-1}), (b) Proposed mechanism of polarization differences in sphere and WSN materials, (c) Yield stresses of ER fluids measured as a function of E field strength (3.0 wt%, 0.1 s^{-1}), and (d) Real time on-off response test of ER fluids.

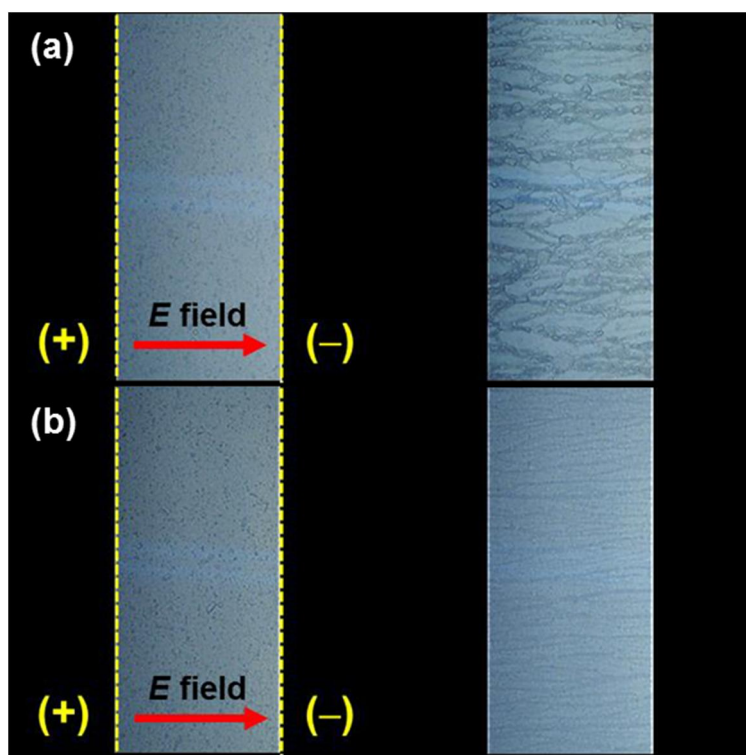


Figure 45. Optical microscope images of practical fibril-like structure formation of (a) W-HNP- and (b) S-HNP-based ER fluids under applied E field strength of 1.0 kV mm^{-1} .

Table 7. Dielectric properties of SiO₂ nanosphere and WSN-derived materials^a

Samples	ϵ_0	ϵ_∞	$\Delta\epsilon=(\epsilon_0-\epsilon_\infty)$	f_{max}^b [Hz]	λ^c [s]
SiO ₂ sphere	3.55	2.85	0.70	48.4	0.0033
S-CSST	4.36	3.01	1.35	98.0	0.0016
S-HNP	4.89	3.08	1.81	238.9	0.00066
WSN	3.95	2.83	1.12	88.3	0.0018
W-CSST	5.23	3.12	2.11	249.1	0.00063
W-HNP	5.75	3.33	2.42	326.2	0.00015

^a Dielectric properties were determined by impedance analyzer (1260, Solatron) coupled with dielectric interface (1296, Solatron).

^b The local frequency of the peak from the dielectric loss factor ϵ'' and the f_{max} values were measured by non-linear regression using OriginPro.

^c The relaxation time was measured using $\lambda=1/(2\pi f_{max})$ relation (f_{max} is the maximum frequency of the loss peak).

4. Conclusion

The monodispersed- hierarchical mesoporous wrinkled silica nanoparticles were successfully fabricated using bicontinuous phase in Winsor III system. Furthermore, as-prepared spherical mesoporous silica nanoparticles presented potential for performance enhancement in applications where silica spheres are currently used. The subtopic is concluded in the view point of each subtopic as follows:

1. Uniform WSNs were successfully fabricated in Winsor III system. Applying the cooling process to the reaction mixture at the appropriate stage of the reaction separated the nucleation and growth stages completely, making it possible to fabricate uniform nanoparticles. Furthermore, the uniformity of the particles was maintained in the experimental conditions, enabling accurate analysis of the factors affecting the sizes and pore sizes of the WSNs. Thus, the method has revealed that it is possible to fabricate uniform WSNs with various sizes and pore sizes by controlling the factors affecting these parameters. This novel method incorporating rapid cooling during the reaction provides a basis for the development of a monodispersed nanoparticle fabrication method. In addition, the CMP performance of

the WSNs compared to silica spheres and a commercial product under the same conditions demonstrated the superiority of the mesoporous structure of the colloidal silica in this application.

2. A simple and reliable strategy to introduce WSNs in DSSCs as scattering layers has been reported. WSN-incorporated cells show a 30.19% greater photovoltaic performance compared with pristine cells. Furthermore, WSNs showed improved light scattering properties compared to non-porous silica nanoparticles of the same size, contributing to 13.76 % PCE enhancement compared with non-porous SiO₂ nanosphere-incorporated cells. This novel approach, which incorporates WSNs in DSSCs for the first time, is expected to advance the application of hierarchical SiO₂ materials to photovoltaic devices for improved performance.

3. W-STCS and W-HNP were successfully fabricated using WSNs as a hard template. TiO₂ shell was coated on WSNs through sol-gel method, and WSN was etched by sonication using NH₄OH solution. W-HNPs manifested higher ER-performance than WSNs and W-STCSs due to the introduction of high dielectric TiO₂ and the hollow structure in

which the silica of the low dielectric was largely decreased. The hierarchical internal surface of the shell of W-HNPs was the unique morphology distinct from S-HNPs, contributing to higher surface area than S-HNPs. In addition, hierarchically arrayed inner surfaces of W-HNP could provide more site for charge accumulations, leading to the high polarizability and ER activity of materials. This reliable approach suggested superiority of spherical mesoporous silica nanoparticles as a hard template and, furthermore, the potential for improved performance in various applications where non-porous silica nanoparticles were applied.

References

- [1] M. Steinhart, *Angew. Chem., Int. Ed.*, 2004, **43**, 2196.
- [2] A.S. Arico, P. Bruce, B. Scrosati, J.-M. Tarascon, and W. van Schalkwijk, *Nat. Mater.*, 2005, **4**, 366.
- [3] A.S. Aricò, P. Bruce, B. Scrosati, J.M. Tarascon, and W. Van Schalkwijk, *Nat. Mater.*, 2005, **4**, 366.
- [4] V.L. Colvin, *Nat. Biotechnol.*, 2003, **21**, 1166.
- [5] G. Yadav, and S. singh, Nanosuspension: A Promising Drug Delivery System, 2012.
- [6] V. Polshettiwar, R. Luque, A. Fihri, H. Zhu, M. Bouhrara, and J.M. Basset, *Chem. Rev.*, 2011, **111**, 3036.
- [7] X. Qu, P.J.J. Alvarez, and Q. Li, *Water Res.*, 2013, **47**, 3931.
- [8] X. Lu, C. Wang, and Y. Wei, *Small*, 2009, **5**, 2349.
- [9] J.N. Coleman, M. Lotya, A. O'Neill, S.D. Bergin, P.J. King, U. Khan, K. Young, A. Gaucher, S. De, R.J. Smith, I.V. Shvets, S.K. Arora, G. Stanton, H.Y. Kim, K. Lee, G.T. Kim, G.S. Duesberg, T. Hallam, J.J. Boland, J.J. Wang, J.F. Donegan, J.C. Grunlan, G. Moriarty, A. Shmeliov, R.J. Nicholls, J.M. Perkins, E.M. Grieveson, K. Theuwissen, D.W. McComb, P.D. Nellist, and V. Nicolosi, *Science*, 2011, **331**, 568.
- [10] H. Jiang, P.S. Lee, and C. Li, *Energy Environ. Sci.*, 2013, **6**, 41.
- [11] A. Albanese, P.S. Tang, and W.C.W. Chan, in: *Annu. Rev. Biomed. Eng.*, 2012, pp. 1.
- [12] M.P. Pileni, *Nat. Mater.*, 2003, **2**, 145.
- [13] R.K. Iler, *The chemistry of silica*, 1979.
- [14] C. Hu, Y. Tang, Z. Jiang, Z. Hao, H. Tang, and P.K. Wong, *Applied Catalysis A, General*, 2003, **253**, 389.
- [15] I.I. Slowing, J.L. Vivero-Escoto, C.W. Wu, and V.S.Y. Lin, *Adv.*

- Drug Delivery Rev.*, 2008, **60**, 1278.
- [16] J.R. Li, R.J. Kuppler, and H.C. Zhou, *Chem. Soc. Rev.*, 2009, **38**, 1477.
- [17] D.J. Bharali, I. Klejbor, E.K. Stachowiak, P. Dutta, I. Roy, N. Kaur, E.J. Bergey, P.N. Prasad, and M.K. Stachowiak, *Proc. Natl. Acad. Sci. U. S. A.*, 2005, **102**, 11539.
- [18] A. Schlossbauer, S. Warncke, P.M.E. Gramlich, J. Kecht, A. Manetto, T. Carell, and T. Bein, *Angew. Chem. Int. Ed.*, 2010, **49**, 4734.
- [19] J. Kobler, K. Möller, and T. Bein, *ACS Nano*, 2008, **2**, 791.
- [20] E.D.E.R. Hyde, A. Seyfaee, F. Neville, and R. Moreno-Atanasio, *Ind. Eng. Chem. Res.*, 2016, **55**, 8891.
- [21] M.A. Malik, M.Y. Wani, and M.A. Hashim, *Arabian Journal of Chemistry*, 2012, **5**, 397.
- [22] M.J. Lawrence, and G.D. Rees, *Adv. Drug Delivery Rev.*, 2000, **45**, 89.
- [23] M.C.A. Stuart, and E.J. Boekema, *Biochimica et Biophysica Acta (BBA) - Biomembranes*, 2007, **1768**, 2681.
- [24] C.T. Kresge, M.E. Leonowicz, W.J. Roth, J.C. Vartuli, and J.S. Beck, *Nature*, 1992, **359**, 710.
- [25] J. Rouquerol, D. Avnir, C.W. Fairbridge, D.H. Everett, J.M. Haynes, N. Pernicone, J.D.F. Ramsay, K.S.W. Sing, and K.K. Unger, in: *Pure Appl. Chem.*, 1994, pp. 1739.
- [26] D. Zhao, Q. Huo, J. Feng, B.F. Chmelka, and G.D. Stucky, *J. Am. Chem. Soc.*, 1998, **120**, 6024.
- [27] F. Tang, L. Li, and D. Chen, *Adv. Mater.*, 2012, **24**, 1504.
- [28] L.F. Giraldo, B.L. López, L. Pérez, S. Urrego, L. Sierra, and M. Mesa, *Macromol. Symp.*, 2007, **258**, 129.
- [29] S.-H. Wu, C.-Y. Mou, and H.-P. Lin, *Chem. Soc. Rev.*, 2013, **42**, 3862.

- [30] S. Perathoner, P. Lanzafame, R. Passalacqua, G. Centi, R. Schlögl, and D.S. Su, *Microporous Mesoporous Mater.*, 2006, **90**, 347.
- [31] H. Yang, N. Coombs, Ö. Dag, I. Sokolov, and G.A. Ozin, *J. Mater. Chem.*, 1997, **7**, 1755.
- [32] R. Ciriminna, A. Fidalgo, V. Pandarus, F. Béland, L.M. Ilharco, and M. Pagliaro, *Chem. Rev.*, 2013, **113**, 6592.
- [33] V. Valtchev, and L. Tosheva, *Chem. Rev.*, 2013, **113**, 6734.
- [34] D. Shen, J. Yang, X. Li, L. Zhou, R. Zhang, W. Li, L. Chen, R. Wang, F. Zhang, and D. Zhao, *Nano Lett.*, 2014, **14**, 923.
- [35] A.B.D. Nandiyanto, S.-G. Kim, F. Iskandar, and K. Okuyama, *Microporous Mesoporous Mater.*, 2009, **120**, 447.
- [36] X. Du, and S.Z. Qiao, *Small*, 2015, **11**, 392.
- [37] Y.-J. Yu, J.-L. Xing, J.-L. Pang, S.-H. Jiang, K.-F. Lam, T.-Q. Yang, Q.-S. Xue, K. Zhang, and P. Wu, *ACS Appl. Mater. Interfaces*, 2014, **6**, 22655.
- [38] V. Polshettiwar, D. Cha, X. Zhang, and J.M. Basset, *Angew. Chem., Int. Ed.*, 2010, **49**, 9652.
- [39] D.-S. Moon, and J.-K. Lee, *Langmuir*, 2012, **28**, 12341.
- [40] B.P. Binks, P.D.I. Fletcher, and L. Tian, *Colloids and Surfaces A: Physicochemical and Engineering Aspects*, 2010, **363**, 8.
- [41] D.-S. Moon, and J.-K. Lee, *Langmuir*, 2014, **30**, 15574.
- [42] P.A. Winsor, *Transactions of the Faraday Society*, 1948, **44**, 376.
- [43] B.P. Binks, *Langmuir*, 1993, **9**, 25.
- [44] R. Nagarajan, and E. Ruckenstein, *Langmuir*, 2000, **16**, 6400.
- [45] B. Davarik, C.W. Koburger, R. Schulz, J.D. Warnock, T. Furukawa, M. Jost, Y. Taur, W.G. Schwittek, J. Debrosse, M.L. Kerbaugh, and J. Mauer, A new planarization technique, using a combination of RIE and chemical mechanical polish (CMP), 1990.
- [46] Y. Chen, Z. Li, J. Qin, and A. Chen, *J. Mater. Sci.*, 2016, **51**, 5811.
- [47] M. Krishnan, J.W. Nalaskowski, and L.M. Cook, *Chem. Rev.*,

2010, **110**, 178.

[48] H. Lei, X. Wu, and R. Chen, *Thin Solid Films*, 2012, **520**, 2868.

[49] H. Li, H. Lei, and R. Chen, *Thin Solid Films*, 2012, **520**, 6174.

[50] D.M. Nelabhotla, T.V. Jayaraman, K. Asghar, and D. Das, *Mater. Des.*, 2016, **104**, 392.

[51] T.G. Deepak, G.S. Anjusree, S. Thomas, T.A. Arun, S.V. Nair, and A. Sreekumaran Nair, *RSC Adv.*, 2014, **4**, 17615.

[52] J.-Y. Liao, B.-X. Lei, D.-B. Kuang, and C.-Y. Su, *Energy Environ. Sci.*, 2011, **4**, 4079.

[53] H.J. Koo, Y.J. Kim, Y.H. Lee, W.I. Lee, K. Kim, and N.G. Park, *Adv. Mater.*, 2008, **20**, 195.

[54] T.-S. Kang, A.P. Smith, B.E. Taylor, and M.F. Durstock, *Nano Lett.*, 2009, **9**, 601.

[55] M.-J. Lee, J.-Y. Park, C.-S. Kim, K. Okuyama, S.-E. Lee, and T.-O. Kim, *J. Power Sources*, 2016, **327**, 96.

[56] W.-Q. Wu, Y.-F. Xu, H.-S. Rao, C.-Y. Su, and D.-B. Kuang, *J. Am. Chem. Soc.*, 2014, **136**, 6437.

[57] Z. Li, Y. Zhou, G. Xue, T. Yu, J. Liu, and Z. Zou, *J. Mater. Chem.*, 2012, **22**, 14341.

[58] S.H. Ahn, D.J. Kim, W.S. Chi, and J.H. Kim, *Adv. Funct. Mater.*, 2014, **24**, 5037.

[59] Q. Zhang, D. Myers, J. Lan, S.A. Jenekhe, and G. Cao, *Phys. Chem. Chem. Phys.*, 2012, **14**, 14982.

[60] T. Hao, *Adv. Mater.*, 2001, **13**, 1847.

[61] T.C. Halsey, *Science*, 1992, **258**, 761.

[62] W. Wen, X. Huang, S. Yang, K. Lu, and P. Sheng, *Nat. Mater.*, 2003, **2**, 727.

[63] J. Yin, X. Zhao, L. Xiang, X. Xia, and Z. Zhang, *Soft Matter*, 2009, **5**, 4687.

[64] F.F. Fang, H.J. Choi, and W.-S. Ahn, *Microporous Mesoporous*

- Mater.*, 2010, **130**, 338.
- [65] B.H. Sung, U.S. Choi, H.G. Jang, and Y.S. Park, *Colloids and Surfaces A: Physicochemical and Engineering Aspects*, 2006, **274**, 37.
- [66] Q. Cheng, V. Pavlinek, Y. He, Y. Yan, C. Li, and P. Saha, *Colloid Polym. Sci.*, 2011, **289**, 799.
- [67] J. Chang, and E.R. Waclawik, *RSC Adv.*, 2014, **4**, 23505.
- [68] Y.-S. Lin, C.-P. Tsai, H.-Y. Huang, C.-T. Kuo, Y. Hung, D.-M. Huang, Y.-C. Chen, and C.-Y. Mou, *Chem. Mater.*, 2005, **17**, 4570.
- [69] B. Zhao, C. Tian, Y. Zhang, T. Tang, and F. Wang, *Particuology*, 2011, **9**, 314.
- [70] S.M. Chang, M. Lee, and W.-S. Kim, *J. Colloid Interface Sci.*, 2005, **286**, 536.
- [71] Y. Song, L.L. Henry, and W. Yang, *Langmuir*, 2009, **25**, 10209.
- [72] H. Yu, P.C. Gibbons, K.F. Kelton, and W.E. Buhro, *J. Am. Chem. Soc.*, 2001, **123**, 9198.
- [73] D.S. Facio, M. Luna, and M.J. Mosquera, *Microporous Mesoporous Mater.*, 2017, **247**, 166.
- [74] E. Yamamoto, S. Mori, A. Shimojima, H. Wada, and K. Kuroda, *Nanoscale*, 2017, **9**, 2464.
- [75] B. Quan, C. Lee, J.S. Yoo, and Y. Piao, *J. Mater. Chem. B*, 2017, **5**, 586.
- [76] J. Wang, A. Sugawara-Narutaki, A. Shimojima, M. Osada, R. Ma, and T. Okubo, *Langmuir*, 2015, **31**, 1610.
- [77] H. Jiang, Z. Zheng, Z. Li, and X. Wang, *Ind. Eng. Chem. Res.*, 2006, **45**, 8617.
- [78] J. Ryu, J. Yun, J. Lee, K. Lee, and J. Jang, *Chem. Commun.*, 2016, **52**, 2165.
- [79] L.M. Rossi, L. Shi, F.H. Quina, and Z. Rosenzweig, *Langmuir*, 2005, **21**, 4277.
- [80] Q. Wang, Y. Liu, and H. Yan, *Chem. Commun.*, 2007, 2339.

- [81] M.P. Nikolić, R. Filipović, and S. Stanojević-Nikolić, *Processing and Application of Ceramics*, 2015, **9**, 209.
- [82] D.J. Belton, O. Deschaume, S.V. Patwardhan, and C.C. Perry, *J. Phys. Chem. B*, 2010, **114**, 9947.
- [83] K.A. Cychosz, R. Guillet-Nicolas, J. Garcia-Martinez, and M. Thommes, *Chem. Soc. Rev.*, 2017, **46**, 389.
- [84] T. Yang, R. Zhou, D.-W. Wang, S.P. Jiang, Y. Yamauchi, S.Z. Qiao, M.J. Monteiro, and J. Liu, *Chem. Commun.*, 2015, **51**, 2518.
- [85] D. Langevin, *Annu. Rev. Phys. Chem.*, 1992, **43**, 341.
- [86] J. Luo, and D.A. Dornfeld, Effects of Abrasive Size Distribution in CMP, in: *Integrated Modeling of Chemical Mechanical Planarization for Sub-Micron IC Fabrication: From Particle Scale to Feature, Die and Wafer Scales*, Springer Berlin Heidelberg, Berlin, Heidelberg, 2004, pp. 97.
- [87] C. Zhou, L. Shan, J.R. Hight, S. Danyluk, S.H. Ng, and A.J. Paszkowski, *Tribol. Trans.*, 2002, **45**, 232.
- [88] Z. Zhang, W. Liu, and Z. Song, *Appl. Opt.*, 2010, **49**, 5480.
- [89] H. Lee, M. Kim, and H. Jeong, *INT J PRECIS ENG MAN*, 2015, **16**, 2611.
- [90] J.C. Yang, D.W. Oh, G.W. Lee, C.L. Song, and T. Kim, *Wear*, 2010, **268**, 505.
- [91] S. Raghavan, M. Keswani, and R. Jia, *KONA POWDER PART J*, 2008, **26**, 94.
- [92] S. Armini, C.M. Whelan, and K. Maex, *Electrochem. Solid-State Lett.*, 2008, **11**, H280.
- [93] Z. Chen, X. Wang, A. Atkinson, and N. Brandon, *J. Eur. Ceram. Soc.*, 2016, **36**, 1435.
- [94] G. Lu, G.Q. Lu, and Z.M. Xiao, *J. Porous Mater.*, 1999, **6**, 359.
- [95] K.S.W. Sing, D.H. Everett, R.A.W. Haul, L. Moscou, R.A. Pierotti, J. Rouquerol, and T. Siemieniewska, *Reporting Physisorption*

Data for Gas/Solid Systems, in: Handbook of Heterogeneous Catalysis, Wiley-VCH Verlag GmbH & Co. KGaA, 2008.

[96] P. Yang, Q. Tang, and B. He, *RSC Adv.*, 2015, **5**, 46260.

[97] P. Cheng, P. Sun, S. Du, Y. Cai, X. Li, Z. Wang, F. Liu, J. Zheng, and G. Lu, *RSC Adv.*, 2014, **4**, 23396.

[98] J. Lee, S.H. Hwang, J. Yun, and J. Jang, *ACS Appl. Mater. Interfaces*, 2014, **6**, 15420.

[99] S. Son, S.H. Hwang, C. Kim, J.Y. Yun, and J. Jang, *ACS Appl. Mater. Interfaces*, 2013, **5**, 4815.

[100] I.G. Yu, Y.J. Kim, H.J. Kim, C. Lee, and W.I. Lee, *J. Mater. Chem.*, 2011, **21**, 532.

[101] J.R. Nagel, and M.A. Scarpulla, *Opt Express*, 2010, **18 Suppl 2**, A139.

[102] S.H. Hwang, J. Yun, and J. Jang, *Adv. Funct. Mater.*, 2014, **24**, 7619.

[103] J.-W. Choi, H. Kang, M. Lee, J.S. Kang, S. Kyeong, J.-K. Yang, J. Kim, D.H. Jeong, Y.-S. Lee, and Y.-E. Sung, *RSC Adv.*, 2014, **4**, 19851.

[104] M. Choi, C. Kim, S. Ok Jeon, K. Soo Yook, J. Yeob Lee, and J. Jang, *Chem. Commun.*, 2011, **47**, 7092.

[105] S. Kim, C. Kim, J.-Y. Hong, S.H. Hwang, and J. Jang, *RSC Adv.*, 2014, **4**, 6821.

[106] W.H. Suh, A.R. Jang, Y.H. Suh, and K.S. Suslick, *Adv. Mater.*, 2006, **18**, 1832.

[107] S.-J. Park, Y.-J. Kim, and S.-J. Park, *Langmuir*, 2008, **24**, 12134.

[108] X.-X. Zhang, B.-B. Xia, H.-P. Ye, Y.-L. Zhang, B. Xiao, L.-H. Yan, H.-B. Lv, and B. Jiang, *J. Mater. Chem.*, 2012, **22**, 13132.

[109] C.-M. Yoon, S. Lee, O.J. Cheong, and J. Jang, *ACS Appl. Mater. Interfaces*, 2015, **7**, 18977.

[110] C.-M. Yoon, S. Lee, S.H. Hong, and J. Jang, *J. Colloid Interface*

Sci., 2015, **438**, 14.

[111] W.L. Zhang, Y.D. Liu, H.J. Choi, and S.G. Kim, *ACS Appl. Mater. Interfaces*, 2012, **4**, 2267.

[112] T. Hao, A. Kawai, and F. Ikazaki, *Langmuir*, 1998, **14**, 1256.

[113] J.-Y. Hong, E. Lee, and J. Jang, *J. Mater. Chem. A*, 2013, **1**, 117.

[114] Y.J. Kim, Y.D. Liu, Y. Seo, and H.J. Choi, *Langmuir*, 2013, **29**, 4959.

[115] H. Block, J.P. Kelly, A. Qin, and T. Watson, *Langmuir*, 1990, **6**, 6.

[116] S.H. Kim, J.H. Kim, H.J. Choi, and J. Park, *RSC Adv.*, 2015, **5**, 72387.

[117] W.L. Zhang, and H.J. Choi, *Langmuir*, 2012, **28**, 7055.

국문초록

다공성 실리카 나노물질은 단위 부피당 표면적이 급격히 증가하여 많은 관심을 받아왔다. 이러한 다공성 구조는 고유한 특성으로 인해 촉매 지지체, 흡착, 분리, 약물 전달, 전극 및 하드 템플레이트와 같은 다양한 응용분야에서 광범위하게 사용된다. 다양한 구조의 다공성 실리카 중에서, 다공성 실리카 나노입자는 우수한 포어 접근성 및 유기적인 분자 확산의 특징을 나타내어 많은 주목을 받고 있다. 그러므로, 다양한 포어 유형의 구조를 갖는 다공성 실리카 나노입자의 많은 제조 방법들이 보고되었으며, 약물 전달, 화장품 및 흡착과 같은 분야의 발전에 기여하였다. 그러나, 이러한 다양한 제조 방법이 보고되고 있지만, 균일하고 고수율의 구형 다공성 실리카 나노입자 제조방법의 발전이 여전히 요구된다.

본 논문에서는 균일한 주름진 구조의 다공성 실리카 나노입자의 제조 방법을 소개한다. 또한, 입자 크기와 기공 크기에 영향을 미치는 인자들을 조사하고, 균일한 주름진 구조의 다공성 실리카 나노입자의 형성 메커니즘을 고찰한다.

최종적으로, 높은 수득률을 가진 다양한 입자 크기 및 기공 크기를 조절할 수 있는 균일한 다공성 주름진 실리카 나노입자의 완성된 방법을 제안한다. 제조한 주름진 구조의 다공성 실리카 나노입자를 화학적 기계적 평탄화 공정의 연마제, 염료 감응형 태양전지의 광 산란 물질 및 전기유변유체의 물질 제조를 위한 하드 템플레이트로 응용하였고, 같은 입자 크기의 비 다공성 실리카 나노구체보다 향상된 성능을 나타내어, 다공성 구조의 우수성을 입증하였다. 본 논문은 다공성 구조를 갖는 실리카 나노입자가 현재 비 다공성 실리카 나노입자가 응용되는 분야에서의 성능 향상을 위한 높은 잠재성을 시사한다.

주요어: 나노입자, 실리카 나노입자, 다공성 실리카 나노입자, 화학적 기계적 평탄화, 태양 전지, 전기유변유체

학 번: 2013-22528